DEVELOPMENT OF A RESONANT-CAVITY-ENHANCED PHOTODETECTOR

DEVELOPMENT OF A Si-BASED RESONANT-CAVITY-ENHANCED INFRARED PHOTODETECTOR

By

ADRIAN GAGNON, B.Sc.

A Thesis

Submitted to the School of Graduate Studies

in Partial Fulfillment of the Requirements

for the Degree

Master of Applied Science

McMaster University

© Copyright by Adrian Gagnon, January 2012

MASTER OF APPLIED SCIENCE (January 2012) McMaster University
(Engineering Physics) Hamilton, Ontario

TITLE: Development of a Si-Based Resonant-Cavity-Enhanced Infrared Photodetector

AUTHOR: Adrian Gagnon

SUPERVISOR: Dr. P. Mascher

NUMBER OF PAGES: viii, 71

Abstract

Resonant-cavity-enhanced (RCE) photodetectors have recently attracted attention due to their wavelength selectivity and high efficiency in comparison to conventional photodetectors. The goal of this ongoing research initiative is to develop a Si-based RCE infrared photodetector using inductively coupled plasma chemical vapor deposition (ICP-CVD) as the primary fabrication method. At the current stage of the project, wavelength-selective optical structures have been successfully fabricated using Si/SiO_2 layer pairs. These structures demonstrate sharp transmission peaks at their intended wavelength, making them potentially useful for efficient photodetection. The next phase of the photodetector development process involves using ion implantation to introduce dopants and create the bias.

The project also explores the temperature sensing capability of the resonant-cavity structures. The temperature sensitivity tests indicate that the specific type of structure fabricated in this project may be relevant for fiber-optic temperature sensing applications. Additional testing is required to evaluate the performance characteristics of such structures as Fabry-Perot sensors capable of wavelength-encoded temperature measurement.

Acknowledgements

My time at McMaster has been an enjoyable and fulfilling experience due to the overwhelming support from numerous people in the Engineering-Physics department. This thesis would not be possible without them. Firstly, I would like to thank my supervisor, Dr. Peter Mascher who has continuously provided guidance and sincere support throughout my degree. Dr. Andy Knights has also provided significant support for my research activities. I would like to send my gratitude to Jacek Wojcik, Evgueni Chelomentsev and Doris Stevanovic who were always willing to take time out of their busy schedules to support my lab work. My research would have been impossible without them.

I am honored to have worked with an excellent network of students in the department. Thanks to members of my research group, Patrick, Ryszard, Dmitrij, Jordan and Kayne for their help with my depositions and other lab work. Special thanks to those outside my group including Dylan Logan, Martin Gerber, Jason Ackert and Stephen Jovanovic who all provided a huge amount of support.

Finally, I would like to thank my parents for their essential support throughout my education.

Contents

Abstract iii

Acknowledgements iv

List of Figures vii

1 Introduction **1**

1.1 Overview and Motivation 1
1.2 Background 2
1.3 Thesis Organization 7

2 Theory and Design **9**

2.1 Optics of Multilayer Thin-Film Structures 9
2.2 The Transfer-Matrix Method 12
2.3 The Resonant Cavity 15
2.4 Design 17

3 Fabrication and Analysis Methods **21**

3.1 Inductively Coupled Plasma Chemical Vapour Deposition 21
3.2 Fourier Transform Infrared Spectroscopy 23
3.3 Ellipsometry 26
3.4 Transmission Electron Microscopy 29

4 Modeling and Calibration Results **32**

4.1 Resonant-Cavity Modeling 32
4.2 Single-Layer Film Tests 37
4.3 Discussion of Modeling and Calibration Results 39

5 Device Analysis Results **42**

5.1 Spectral Measurements Using FTIR 42
5.2 TEM Imaging 45

5.3 Thickness Compensation....................48
5.4 Discussion of Structure Analysis Results....................50

6 Temperature Sensing Applications....................52

6.1 Background....................52
6.2 Sensitivity Tests....................54
6.3 Discussion of Temperature Sensitivity Results....................57

7 Conclusion and Future Work....................60

References 66

List of Figures

Figure 2.1: Constructive interference of reflected beams within a dielectric mirror. .10

Figure 2.2: Typical reflectivity spectrum for a dielectric mirror. 11

Figure 2.3: Propagation of a beam incident on a single layer. The direction perpendicular to the plane of incidence is denoted using a bold dot [29]. 13

Figure 2.4: Fabry-Perot etalon consisting of parallel reflecting plates separated by distance d. 17

Figure 2.5: Design concept for a resonant-cavity structure composed of *a*-Si and SiO_2. 18

Figure 2.6: RCE photodetector design including implanted Boron and Phosphorus regions along with the metal contacts. 19

Figure 3.1: Diagram of the ICP-CVD system at McMaster University. 22

Figure 3.2: The Michelson interferometer. 24

Figure 3.3: The FTIR process chain. 25

Figure 3.4: Reflection and transmission of a beam incident on a sample interface. ...27

Figure 3.5: Typical setup for monochromatic ellipsometry. 27

Figure 3.6: (Left) TEM schematic in diffraction mode. (Right) TEM schematic in imaging mode 30

Figure 3.7: Philips CM12 conventional analytic TEM operating at 120kV 31

Figure 4.1: 14-layer resonant-cavity structure composed of alternating *a*-Si/SiO_2 layers. 33

Figure 4.2: Simulated reflectivity spectrum for the structure depicted in Figure 4.1. 33

Figure 4.3: Simulated comparison of reflectivity spectra in relation to the number of layers. 35

Figure 4.4: Simulated reflectivity spectra with varying thickness of the half-wave layer. 35

Figure 4.5: Simulated reflectivity spectra showing the detrimental effect of excess variation of the middle-layer thickness 36

Figure 4.6: Simulated reflectivity spectra showing ±10 nm random variation of all layer thicknesses..37

Figure 4.7: Measured RI for a single layer of *a*-Si deposited at 500ºC.....................388

Figure 4.8: Measured RI for a single layer of SiO_2 deposited at 500ºC......................39

Figure 5.1: 14-layer resonant-cavity structure deposted on a Si substrate at 700ºC ...42

Figure 5.2: Measured reflectivity spectra for as-deposited and annealed samples of resonant-cavity structure depicted in Figure 5.1. 43

Figure 5.3: 10-layer resonant-cavity structure deposted on a Si substrate at 700ºC ...44

Figure 5.4: Measured reflectivity spectra for as-deposited and annealed samples of the resonant-cavity structure depicted in Figure 5.3. 45

Figure 5.5: TEM image of the a 14-layer structure. 46

Figure 5.6: TEM image showing a three-layer section of the resonant cavity structure. The darker layers are *a*-Si. 47

Figure 5.7: TEM image of the *a*-Si/SiO_2 layer interface. 48

Figure 5.8: Measured reflectivity spectrum for the thickness-compensated structure. 49

Figure 6.1: Simulated temperature sensitivity of the resonant-cavity structure using 15 degree intervals...55

Figure 6.2: Tunable laser setup used for temperature sensitivity testing. 56

Figure 6.3: Measured reflectivity sperctra of the resonant-cavity structure with increasing temperature. 57

Figure 7.1: Resonant-cavity structure after upper-layer etching. 62

Figure 7.2: Resonant-cavity structure with upper layers removed for clarity, revealing interdigitated doped regions. 64

Chapter 1

Introduction

1.1 Overview and Motivation

Modern optical communication systems require high-performance components to satisfy the demand for faster, more efficient and reliable networking. Since the 1990s, there has been interest in devices which rely on resonant cavity effects to enhance performance. Specifically, resonant-cavity-enhanced (RCE) photodetectors have received significant attention, and several studies have demonstrated various degrees of enhancement in comparison to previous generations of photodetectors [1-6]. Typically, semiconductor photodetectors require a large absorption region for sufficient light collection. With a larger absorption region the transit time is increased, resulting in a speed decrease. Therefore, the trade-off between efficiency and speed is a limiting factor for conventional photodetectors [7, 8]. By exploiting the properties of a resonant cavity this trade-off can be avoided. The cavity serves to enhance the light field at a specific wavelength within the absorption region. This enhancement enables efficient light absorption even with a thin absorption region.

Resonant-cavity enhancement also enables wavelength selectivity, meaning the photodetector is highly sensitive at a specific wavelength while remaining unresponsive to off-resonance wavelengths. Wavelength selectivity is an attractive characteristic for low crosstalk wavelength division multiplexing (WDM). WDM is an essential technology that serves to increase the capacity of optical communication systems [9].

This thesis describes the progress of an ongoing research initiative to develop a Si-based RCE photodetector operating at 1550 nm. The primary focus thus far has been to fabricate multilayer thin-film microcavity structures using Inductively Coupled Plasma Chemical Vapour Deposition (ICP-CVD). These optical structures are composed of alternating amorphous silicon (*a*-Si) and SiO_2 layers. The reflective and transmissive characteristics of such film structures are dependent on the interference of light throughout the layers. These microcavity structures have been successfully fabricated and exhibit the desired optical characteristics necessary for an infrared RCE photodetector. The thesis describes in detail the essential research stages including device design, modeling, fabrication and analysis.

1.2 Background

Many of the fundamental physical concepts required for RCE devices have been known for over a century. At the end of the 19th century, Charles Fabry and Alfred Perot developed the Fabry-Perot etalon, consisting of two reflecting surfaces placed in parallel. The transmission spectrum of an etalon is highly dependent on the wavelength of incident

light, and transmission peaks occur at the resonances of the etalon. This interferential phenomenon has since resulted in numerous applications, especially in optical device technology [10]. In terms of the RCE photodetector, the resonant cavity is essentially a Fabry-Perot etalon where the resonance condition of the etalon is the operating wavelength of the photodetector.

The first application of resonant-cavity enhancement in semiconductor devices occurred in 1976 at Philips Research Laboratories [11]. Goedbloed and Joosten demonstrated a photodiode that exhibited interference ripples in its responsivity when illuminated with light of varying wavelength. The researchers verified that the interference was due to multiple reflections between the front and back contacts of the diode. This discovery sparked a new interest in devices that exploit the properties of a resonant cavity. Advancements in crystal growth technology throughout the late 1900s have enabled researchers to experiment with various materials and more complex device designs. Many research groups have since been pursuing RCE photodetectors for high-performance applications at wavelengths ranging from visible to mid-infrared [9].

Throughout the initial stages of RCE detector research, one of the most commonly studied material systems was AlGaAs/GaAs/InGaAs [9]. These materials exhibit reasonable electronic properties, and alloys can easily be grown by Molecular Beam Epitaxy (MBE). GaAs/AlAs mirrors are capable of functioning at telecommunication wavelengths; yet, the majority of applications are in the range of 850 - 950 nm [12-14]. The sensitivity range of GaAs based detectors can be extended to 1550 nm by using the

AlAs/GaAs/Ge material system. Ge has a low recombination rate and a reasonable absorption coefficient for this wavelength range [15, 16].

InP/InGaAs/InAlAs is also a suitable material system for telecommunications wavelengths [17, 18]. However, InGaAs and InAlAs have a low refractive index (RI) contrast, meaning more periods are required to achieve high reflectivity, and thus a high-quality cavity. Lattice-matched InGaAs also has a bandgap close to 1550 nm, and therefore InGaAs/InAlAs mirrors are limited to longer wavelengths. InGaAlAs/InGaAsP mirrors must instead be used for the 1550 nm range [15].

Si-based detectors are particularly attractive for their potential integration with Si electronics. Generally, Si detectors are limited to operating wavelengths shorter than 1 μm. The use of SiGe can extend the functionality of these detectors to longer wavelengths [19, 20]. Mirrors fabricated using SiGe/Si have drawbacks including the RI contrast and light absorption by SiGe in the wavelength range of interest. Si/SiO_2 is an effective combination for high efficiency devices. The index contrast is high and fewer periods are needed to fabricate mirrors with near-unity reflectivity. Given the bandgap of Si, the active region should contain dopants or other absorbing materials for operation in the 1.5 μm range.

Other material combinations have been explored for photodetectors operating outside the telecommunication wavelength range. These include Si/AlP/GaP for detection of blue light at 520 nm [16], and the combination of AlAsSb/GaInAsSb/GaSb for wavelengths greater than 2 μm [21].

In recent years, several research groups have successfully applied RCE based techniques to enhance the detection capabilities of various detector types. Among the first reported RCE detectors was a Schottky photodiode realized by Chin and Chang who placed a conventional Schottky diode in a resonant cavity resulting in a 50% enhancement of detected photocurrent [22]. RCE avalanche photodiodes have also been realized by research groups such as Kuchibholta *et al*. who used a 15-period AlAs/GaAs stack as a bottom mirror to enhance the absorption in a thin InGaAs layer [23]. However, the low reflectivity of the bottom mirror limited the quantum efficiency to 49%. p-i-n photodiodes have received significant attention as candidates for high-speed detectors operating at over 100 GHz. This type of photodetector is capable of overcoming the bandwidth-sensitivity trade-off which is common among conventional photodetectors. Other RCE photodetector types have been realized including heterojunction phototransistors and metal-semiconductor-metal (MSM) photodetectors [24][25][9].

More recently, multiple groups have investigated the use of wafers with buried reflectors as the bottom mirror. In 2000, Qiming *et al*. reported on an MBE-deposited SiGe/Si multiple quantum well RCE photodetector fabricated on a separation-by-implanted-oxygen (SIMOX) wafer [26]. In this case, the top mirror was fabricated using Si/SiO_2 layers, whereas the buried oxide layer in the SIMOX wafer acted as the bottom mirror with a reflectance of 80%. The full width at half maximum was found to be 14 nm, with an external quantum efficiency of 2.9% at the design wavelength of 1300 nm. Due to

the design, the device speed was limited to approximately 1-2 GHz. The authors suggested a smaller device area to improve speed.

Unlu and Emsley have specifically studied epitaxy-ready reflecting substrates [27]. In 2000, they introduced a commercially reproducible silicon wafer with a buried Distributed Bragg Reflector (DBR) for Si photodiodes operating in the 800 – 900 nm range. Wafers were manufactured using DBR structures with reflectance values in excess of 90% using only two Si/SiO_2 periods. After the buried DBR fabrication, crystalline Si was grown on the Si surface. At the point of minimum reflectivity – or highest quantum efficiency – the reflectance was reduced to less than 40%, allowing for a potential photodiode quantum efficiency greater than 50%. However, the authors encountered difficulty controlling the exact wavelength at which the peak quantum efficiency occurred. Li and Yang also reported on Si wafers with buried Si/SiO_2 reflectors [1]. In this case, reflectance near 100% was achieved, and the authors predicted a ten-fold improvement in quantum efficiency in comparison to conventional photodetectors.

The characteristics of resonant-cavity structures can be exploited for other optical sensing devices. Specifically, Unlu *et al*. have explored the usage of Si/SiO_2 structures for biological imaging applications [28]. For this application, two Bragg mirrors composed of Si and SiO_2 are positioned facing each other so as to form an optical cavity. A tunable laser is used to sweep the incident wavelength near the resonance condition. Transmitted light is then spatially imaged on a camera beyond the cavity. The resonance condition along the length of the cavity of the device is dependant on the position of certain

combinations of biomolecules. Essentially, the presence of these biomolecules is detected by a minor perturbation of the electric field. This effect is greatly enhanced by the presence of the resonant cavity. Therefore, the sensitivity is amplified in comparison to conventional interference techniques. According to the authors, the setup is inexpensive to construct and operate. It should also be noted that these Bragg reflectors are based on well-known Si-processing technology, so the setup can be made inexpensive enough for disposable, one-time use devices.

1.3 Thesis Organization

The project is outlined phase by phase, from device design and modeling to fabrication and analysis. Chapters 1-2 give the background and theory that are useful in understanding the development process. Chapter 3 outlines the methods for fabrication and analysis of the resonant-cavity structures. Chapter 4 describes the initial modeling that was used to investigate the optical characteristics in relation to the physical parameters of the structures. Chapter 4 also outlines the preliminary test results on single-layer films. These tests were used to calibrate the fabrication of multilayer structures. Chapter 5 presents an overview of the device analysis results, including spectral plots obtained by Fourier Transmission Infrared Spectroscopy (FTIR) and images of the structures obtained from Transmission Electron Microscopy (TEM). Chapter 6 describes the potential temperature sensing applications of the microcavity structures. Chapter 7

presents a summary of the experimental results and outlines the future steps in the development of the RCE photodetector.

Chapter 2

Theory and Design

2.1 Optics of Multilayer Thin-Film Structures

This project deals primarily with the design and fabrication of resonant microcavity structures that act as precise optical filters. These structures are composed of multiple layers of semiconductor or dielectric films which are deposited on a substrate. The optics of multilayer thin-film structures is therefore an essential component to this research. An overview of this component is presented in this section.

For a multilayer thin-film structure, the reflectance and transmittance characteristics are dependent on the physical characteristics of the structure including layer thicknesses and refractive indices. Figure 2.1 presents an example of a stack of dielectric films with refractive indices n_1 and n_2. A beam incident on the stack will undergo partial reflection at the interface between the ambient medium and the first layer. The transmitted portion

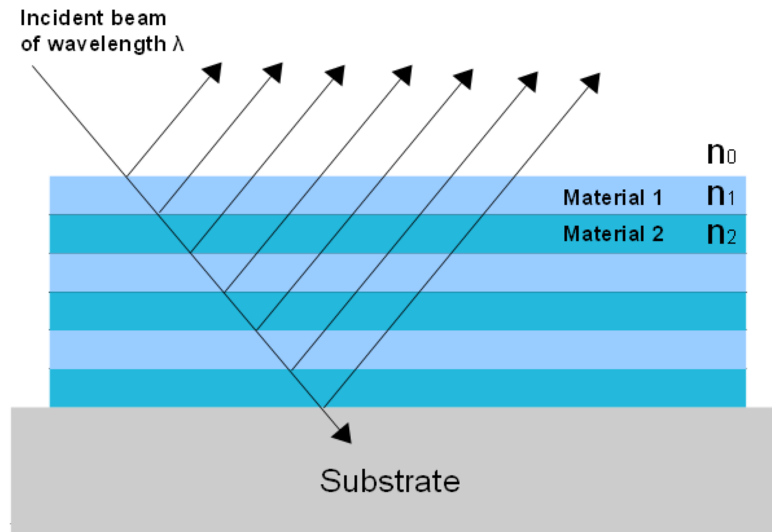

Figure 2.1: Constructive interference of reflected beams within a dielectric mirror.

will also be partially reflected at the interface of layers 1 and 2. If this initial process is expanded to the entire stack, the series of reflected and transmitted beams will undergo interference, which in effect influences the overall reflectance and transmittance of the stack. By careful tuning of the physical characteristics of a dielectric stack, highly reflective and anti-reflective films can be realized. If the optical thickness of each layer is equal to one-quarter the wavelength of the incident light, the reflected beams from each interface will be in phase, resulting in constructive interference [29]. Such a structure is often referred to as a Distributed Bragg Reflector (DBR), Bragg Mirror, or a Dielectric Mirror. The reflectivity spectrum for a dielectric mirror is shown in Figure 2.2.

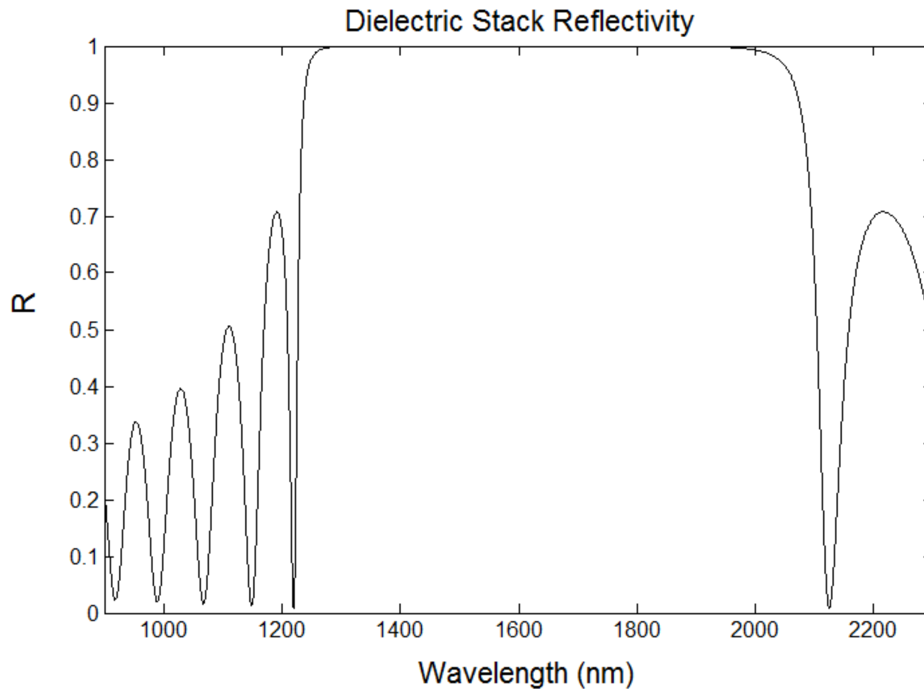

Figure 2.2: Typical reflectivity spectrum for a dielectric mirror.

The plot shows a distinct resonance region in which the reflectivity is near unity. For this wavelength range, the constructive interference condition is satisfied. The above example may also be considered as a one-dimensional photonic crystal. The periodic nature of a photonic crystal is similar to that of a semiconductor crystal; however, instead of influencing electron motion, a photonic crystal influences the propagation of electromagnetic waves [29]. In the photonic-crystal approach, the region of high reflectivity acts as a forbidden energy band. Light which has a wavelength within this energy band is forbidden from propagating within the structure.

2.2 The Transfer-Matrix Method

Multilayer structures such as dielectric mirrors have many industrial applications including highly-reflective mirrors for gas lasers and anti-reflective lens coatings on optical instrumentation [29]. For optimal design of such structures, a mathematical formulation is needed to determine the performance characteristics. When dealing with a small number of layers, it may be sufficient to approach the problem directly by calculating the sum of the reflected and transmitted beams to determine the overall reflectance and transmittance. This method becomes increasingly complicated for more complex structures. Instead, a more efficient technique called the transfer-matrix method is preferable. A mathematical outline of the transfer-matrix method is presented in this section.

Maxwell's equations are the foundation of the transfer-matrix method. The complex series of reflected and transmitted beams can be considered already accounted for in the electric fields that satisfy the boundary conditions required by Maxwell's equations. Figure 2.3 depicts a beam incident on a homogeneous, isotropic film with thickness comparable to the wavelength of the incident light. A specific terminology is used to account for multiple reflections in the interference. E_{r1}, for example, represents the sum of all reflected beams in the process of emerging from the film, incident on interface (a). The boundary conditions at interfaces (a) and (b) can be written as

$$E_a = E_0 + E_{r1} = E_{t1} + E_{i1} \tag{2.1}$$

$$E_b = E_{i2} + E_{r2} = E_{t2} \tag{2.2}$$

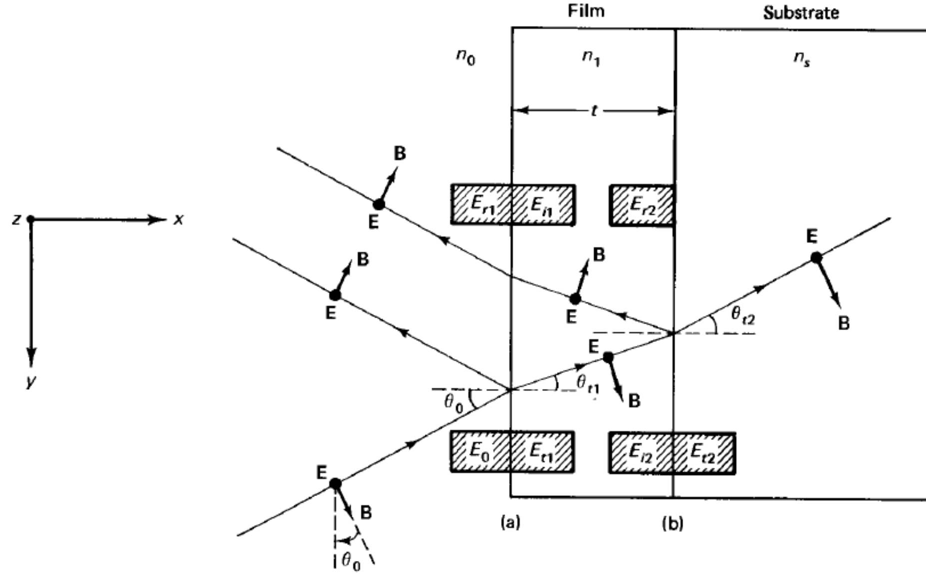

Figure 2.3: Propagation of a beam incident on a single layer. The direction perpendicular to the plane of incidence is denoted using a bold dot [29].

$$B_a = B_0 \cos\theta_0 - B_{r1} \cos\theta_0 = B_{t1} \cos\theta_{t1} - B_{i1} \cos\theta_{t1} \tag{2.3}$$

$$B_b = B_{i2} \cos\theta_{t1} - B_{r2} \cos\theta_{t1} = B_{t2} \cos\theta_{t2} \tag{2.4}$$

The electric and magnetic fields are related by

$$B = \frac{E}{v} = \left(\frac{n}{c}\right) E = n\sqrt{\epsilon_o \mu_o} E \tag{2.5}$$

Equation (2.5) is combined with the interface boundary conditions to yield

$$B_a = \gamma_0 (E_0 - E_{r1}) = \gamma_1 (E_{t1} - E_{i1}) \tag{2.6}$$

$$B_b = \gamma_1 (E_{i2} - E_{r2}) = \gamma_s E_{t2} \tag{2.7}$$

where γ_0 and $\gamma_1$are defined as

$$\gamma_0 \equiv n_0\sqrt{\epsilon_o\mu_o}\cos\theta_0 \tag{2.8}$$

$$\gamma_1 \equiv n_1\sqrt{\epsilon_o\mu_o}\cos\theta_{t1} \tag{2.9}$$

$$\gamma_s \equiv n_s\sqrt{\epsilon_o\mu_o}\cos\theta_{t2} \tag{2.10}$$

It should be noted that in the case of the other polarization, where E is chosen in the original direction of B, the cosine factors appear in the denominator as opposed to the numerator. The electric and magnetic fields at the film interface a can further be simplified to

$$E_a = E_b\cos\delta + B_b\left(\frac{i\sin\delta}{\gamma_1}\right) \tag{2.11}$$

$$B_a = E_b(i\gamma_1\sin\delta) + B_b\cos\delta \tag{2.12}$$

$$E_b = E_{t1}e^{-i\delta} + E_{i1}e^{i\delta} = E_{t2} \tag{2.13}$$

$$B_b = \gamma_1(E_{t1}e^{-i\delta} + E_{i1}e^{i\delta}) = \gamma_s E_{t2} \tag{2.14}$$

where the path difference δ is defined as

$$\delta = k_0\Delta = \left(\frac{2\pi}{\lambda_0}\right)n_1 t\cos\theta_{t1} \tag{2.15}$$

The set of E and B equations can be related using the following matrix equation

$$\begin{bmatrix} E_a \\ B_a \end{bmatrix} = \begin{bmatrix} \cos\delta & \frac{i\sin\delta}{\gamma_1} \\ i\gamma_1\sin\delta & \cos\delta \end{bmatrix}\begin{bmatrix} E_b \\ B_b \end{bmatrix} \tag{2.16}$$

$$\begin{bmatrix} E_a \\ B_a \end{bmatrix} = \mathrm{M_1M_2M_3 \dots M_N}\begin{bmatrix} E_N \\ B_N \end{bmatrix} \tag{2.17}$$

$$\mathrm{M_T} = \mathrm{M_1M_2M_3 \dots M_N} \tag{2.18}$$

The transmission and reflection coefficients t and r can be written in terms of the transfer matrix elements as

$$t = \frac{2\gamma_0}{\gamma_0 m_{11} + \gamma_0 \gamma_s m_{12} + m_{21} + \gamma_s m_{22}} \tag{2.19}$$

$$r = \frac{\gamma_0 m_{11} + \gamma_0 \gamma_s m_{12} - m_{21} - \gamma_s m_{22}}{\gamma_0 m_{11} + \gamma_0 \gamma_s m_{12} + m_{21} + \gamma_s m_{22}} \tag{2.20}$$

where the elements of $\mathrm{M_T}$ are as follows

$$m_{11} = \cos\delta \tag{2.21}$$

$$m_{12} = \frac{i \sin\delta}{n_1 \sqrt{\epsilon_0 \mu_0}} \tag{2.22}$$

$$m_{21} = i n_1 \sqrt{\epsilon_0 \mu_0} \sin\delta \tag{2.23}$$

$$m_{22} = \cos\delta \tag{2.24}$$

These equations are simplified further in the case of normal incidence. In this case the cosine factors are all unity. The reflectance R at normal incidence can then be written as

$$R = \frac{n_1^2 (n_0 - n_s)^2 cos^2\delta + (n_0 n_s - n_1^2)^2 sin^2\delta}{n_1^2 (n_0 + n_s)^2 cos^2\delta + (n_0 n_s + n_1^2)^2 sin^2\delta} \tag{2.25}$$

For unpolarized light at oblique incidence, an average can be taken for both polarizations.

2.3 The Resonant Cavity

The theoretical foundation described above can be applied to the design of multilayer film structures to achieve very specific optical characteristics. The reflectivity spectrum of a DBR structure can be significantly altered by breaking the periodicity. For

example, if a single quarter-wave layer in the middle of the structure is replaced with a half-wave layer, the interference conditions within the structure are altered. The result is a distinct transmission peak at a specific resonant wavelength. Such a structure can alternately be considered as a photonic crystal. In this case, the periodicity of the one-dimensional photonic crystal is interrupted by the half-wave layer. Analogous to the effect of introducing a defect in an atomic crystal, the half-wave layer acts as a defect in the photonic crystal and therefore affects the propagation of light within the structure. The defect essentially creates an allowable energy level within the forbidden region which corresponds to the energy of the wavelength at which the transmission peak occurs.

Aside from the photonic crystal approach, it is necessary to outline the optical phenomenon involved. From an optics perspective the half-wave layer acts as a resonant cavity, or more specifically a Fabry-Perot etalon which has been briefly described in Chapter 1. The cavity of a Fabry-Perot etalon is confined by two reflecting plates, which in this case are replaced by two DBRs on opposite sides of the half wave layer. The Fabry-Perot etalon concept is summarized in Figure 2.4. Light travelling through the structure undergoes multiple reflections when it enters the half-wave layer, which can be considered as a resonant cavity. The light field is amplified within this region, making such structures ideal for absorption efficiency enhancement.

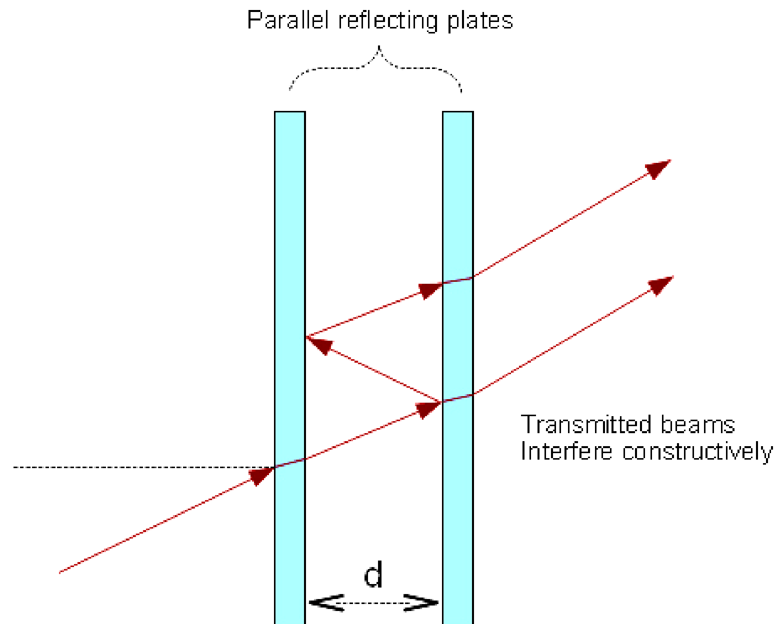

Figure 2.4: Fabry-Perot etalon consisting of parallel reflecting plates separated by distance d.

2.4 Design

The primary objective of this research initiative to date has been the fabrication of multilayer film resonant-microcavity structures that could be used in the design of a RCE infrared photodetector. The multilayer structures ideally should be compatible with conventional silicon fabrication technology and able to demonstrate the characteristics necessary to potentially enhance the speed and efficiency of a photodetector. The enhancement should apply to the operating wavelength only, while the performance at other wavelengths will remain unaffected. The general film structure described in the

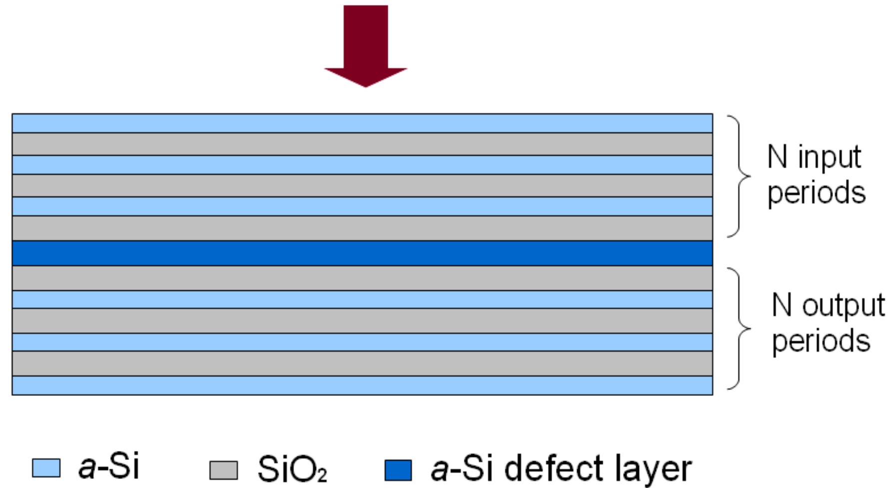

Figure 2.5: Design concept for a resonant-cavity structure composed of *a*-Si and SiO_2.

previous section is an appropriate starting point for meeting these requirements. The basic design is depicted in Figure 2.5. This structure is composed of only two materials which are arranged in alternating layers. *a*-Si and SiO_2 are suitable materials given their RI contrast. At 1550 nm the measured RI of *a*-Si and SiO_2 are 3.30 and 1.45, respectively. These materials are also readily available via ICP-CVD. The structure is essentially a one-dimensional photonic crystal whose periodicity is interrupted by a half-wave defect layer. From an optics perspective, the structure is a Fabry-Perot etalon with two dielectric mirrors on either side of the half-wave layer.

The type of structure depicted in Figure 2.5 acts as a precise optical filter, allowing only light at a specific wavelength to pass through. The light field is also enhanced within the half-wave layer due to multiple internal reflections. The half-wave

layer is therefore an ideal candidate for the absorbing layer, should the structure be used as a photodetector. The half-wave layer can be thin in comparison to conventional detectors given that light will have multiple passes within the absorption region. At the intended operating wavelength of 1550 nm, Si is typically non-absorbing. If the structure is to be used as a photodetector, the absorbing layer would be doped using ion implantation.

Figure 2.6 depicts a potential design for a photodetector made from a resonant-cavity structure. The upper mirror of the original structure would be etched such that ion-implanted n+ and p+ regions can be introduced. The electrode penetrates into the absorption layer to allow for maximum collection. This design allows for an arbitrarily large area (the size of a beam spot size) to be nearly completely depleted so that all generated carriers may be extracted efficiently. The doped regions would be made sufficiently thin to ensure that free-carrier absorption loss has a minimal effect compared to loss associated with deep levels. The doped regions do not have a dielectric stack

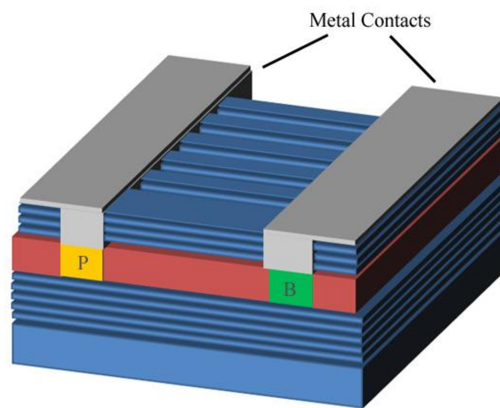

Figure 2.6: RCE photodetector design including implanted Boron and Phosphorus regions along with the metal contacts.

above them, so the light generally will not be confined there. The spacing of the doped regions will depend on the carrier lifetime. Essentially, the spacing should be on the order of the electron diffusion length.

If the number of periods on the back mirror is increased, the transmission spectrum will be reduced to zero, while the absorption spectrum essentially takes on the form of the transmission spectrum within the symmetric cavity. It is possible, for a given absorption coefficient of silicon, to choose the number of periods for the top mirror that will result in near 100% absorption at resonance.

Chapter 3

Fabrication and Analysis Methods

3.1 Inductively Coupled Plasma Chemical Vapour Deposition

Chemical Vapour Deposition technology has become an essential element within the semiconductor industry. The process was first developed for practical use in the 1880s for the purpose of coating lamp filaments with carbon or metal to improve strength. The importance of CVD coatings grew rapidly after World War II. The technology continues to expand at an increasing rate [30].

CVD is defined by Pierson as "The deposition of a solid on a heated surface from a chemical reaction in the vapour phase" [31]. For the deposition of multilayer thin-film structures in this research, the specific CVD method employed was inductively coupled plasma chemical vapour deposition. This method involves an inductive circuit element adjacent to a discharge region such that the energy from an RF power source is coupled to an ionized gas. The circuit element is generally a conductor in the shape of a spiral or helix [31, 32]. The ICP-CVD system at McMaster University was used to fabricate all resonant-cavity structures in this research. A system diagram of the ICP-CVD is given in

Figure 3.1. For each deposition the full structure design was programmed into the automated interface to ensure that the deposition would take place without any manual interchanges of gases. An Ar source was used as the plasma gas. The silicon source gas was 30% SiH_4 in Ar. 10% O_2 in Ar was used as the oxygen source. A 120 second buffer stage was implemented between each layer to allow for full gas interchange. The wafer was shielded during the interchange stages. All depositions were calibrated for 700ºC and were performed with a chamber base pressure of 2×10^{-8} Torr. The RF power was maintained at 300 W.

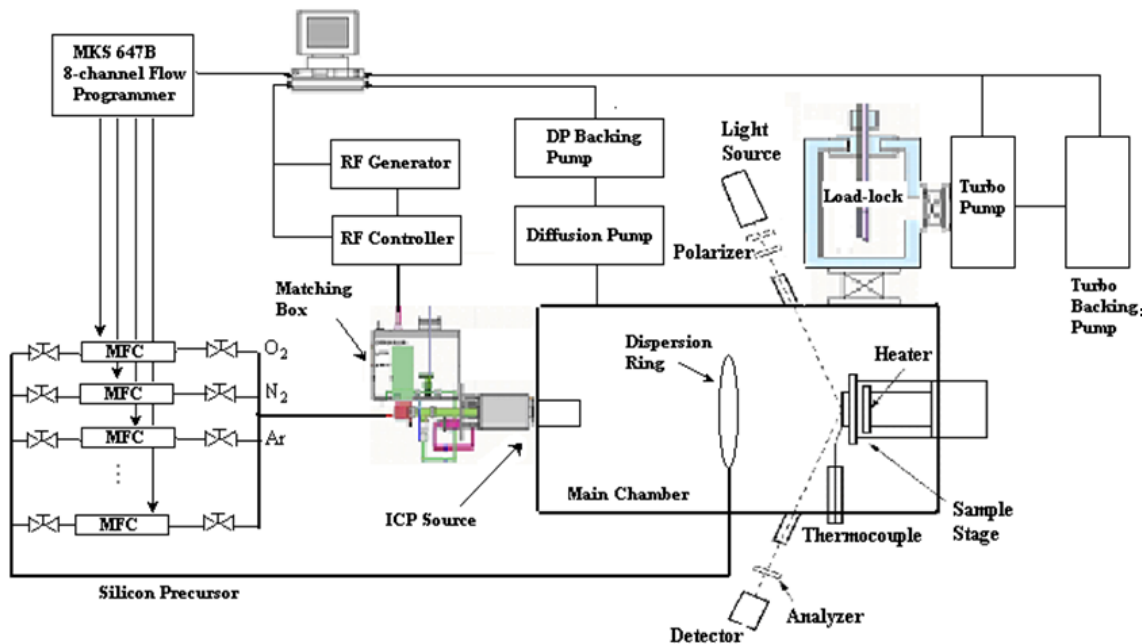

Figure 3.1: Diagram of the ICP-CVD system at McMaster University [33].

3.2 Fourier Transform Infrared Spectroscopy

The reflectance and transmittance characteristics of the multilayer structures deposited in this study were investigated using Fourier Transform Infrared Spectroscopy (FTIR). This method enables efficient measurement of the optical spectrum over a wide wavelength range covering the entire resonance region wherein the reflectance is near-unity. Fourier-Transform Spectroscopy employs a Michelson interferometer to simultaneously process the entire spectral range during a single scan. This aspect is called the Multiplex advantage, which separates the technique from more limited methods such as prism or grating spectrometry. The Michelson interferometer is shown in Figure 3.2. A beam splitter is used to separate the input light into equal parts which are then recombined by the beam splitter before reaching the detector. The separated beams are reflected by their respective mirrors before returning to the beam splitter, thereby introducing a path difference dependent on the frequency of the incident light.

In the process of FTIR, an interferogram is measured by varying the position of the interferometer mirror. Each interferogram data point contains information about all frequencies originating from the light source.

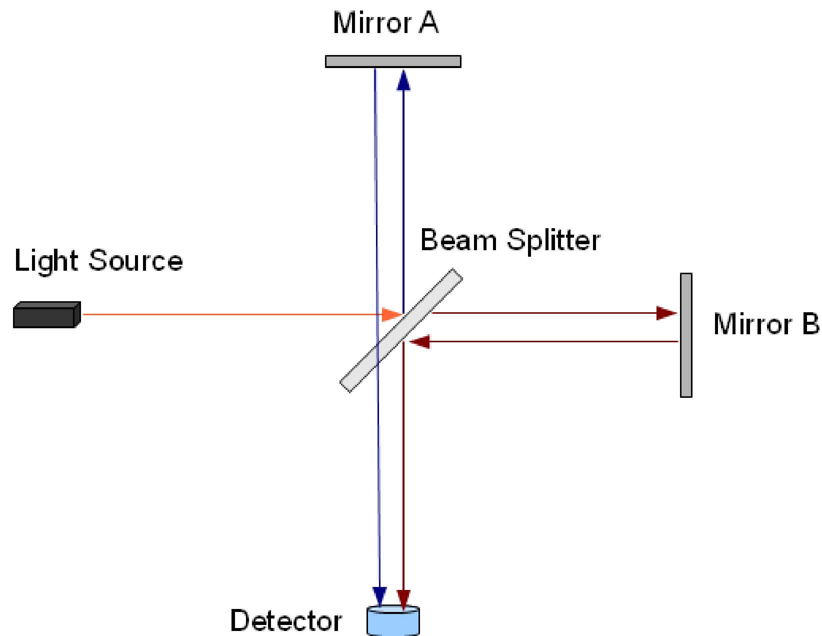

Figure 3.2: The Michelson interferometer.

Figure 3.3 outlines the typical process chain for FTIR measurements. Light emitted from the source initially passes through the interferometer. The interferometer output then passes through the sample, altering the interferogram depending on the sample properties. A detector collects the light to conclude the spectrometry process. By using the well-known technique of Fourier transform, the interferogram is converted to a spectrogram via computer.

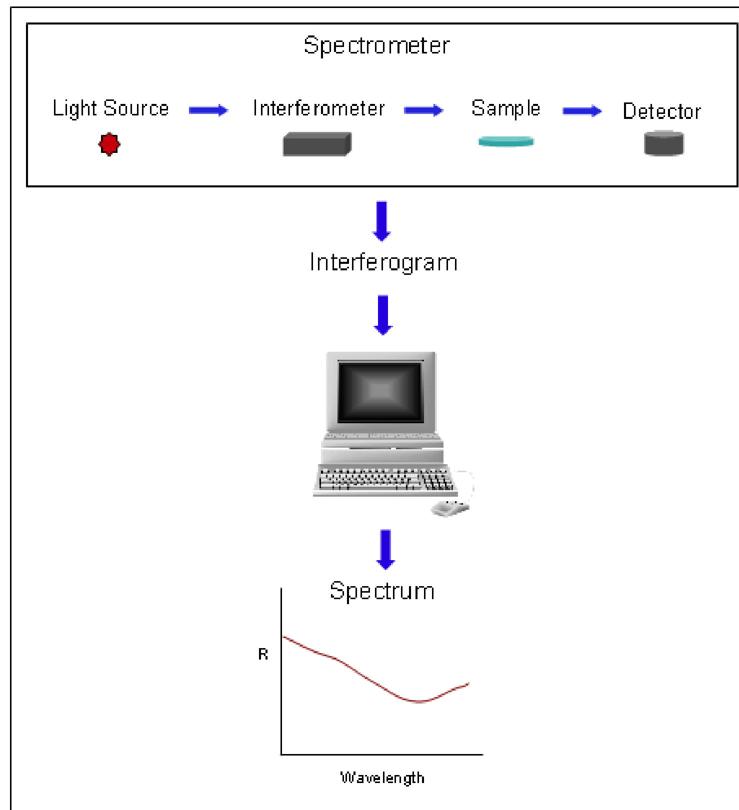

Figure 3.3: The FTIR process chain.

In this project, FTIR was employed as the primary method of analyzing the reflective and transmissive characteristics of the resonant-cavity structures. For all measurements, the sample was contained in a closed chamber isolated from room lighting. Measurements were performed at room temperature with air surrounding the sample. Before each sample measurement the background spectrum was measured as a reference for 100% transmission. The spectrum obtained with the sample in the chamber was normalized using the background spectrum, yielding the transmission spectrum of the sample. The reflectance spectra were calculated under the assumption that any light not

transmitted to the detector was reflected. All measurements were performed at normal incidence. The output spectra for all samples contained transmission information for wavelengths within the range of 800 - 8000 nm.

3.3 Ellipsometry

Section 4.2 deals with single-layer CVD-deposited a-Si and SiO_2 thin films. The optical properties of these films were analyzed using ellipsometry; a well established technique for thin-film analysis. The term ellipsometry was coined by Rothen in 1945 [34], however, the technique is based on Drude's work decades earlier, published at end of the 19th century [35]. Initially, little attention was given to Drude's work until the 1970s and 1980s during which the technique became widely utilized.

In general, ellipsometry deals with changes in the polarization state of light after being reflected from the sample surface. The complex ratio of the linearly independent electric field components is determined. Figure 3.4 illustrates the change in polarization of a beam upon reflection from a surface. An ellipsometric measurement generally results in real valued parameters Ψ and Δ, where $\tan(\Psi)$ is the absolute value of the complex ratio of the electric field components, and Δ is the phase change of the electric field vector components. Ellipsometry is a non-invasive and non-destructive tool. For this reason is has become a useful technique for *in-situ* measurements [36].

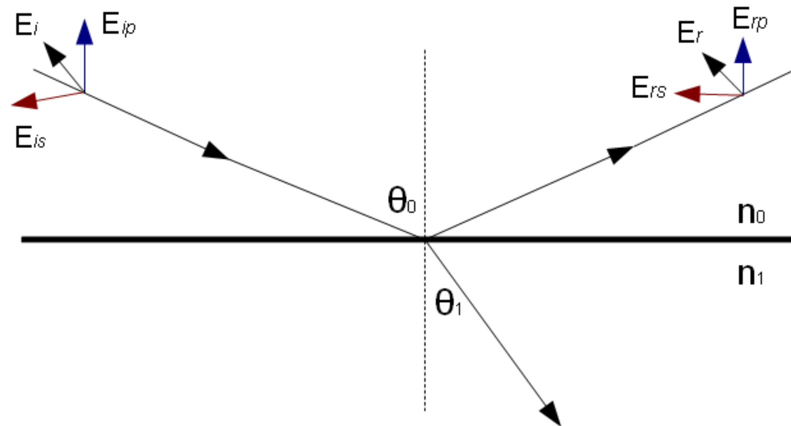

Figure 3.4: Reflection and transmission of a beam incident on a sample interface.

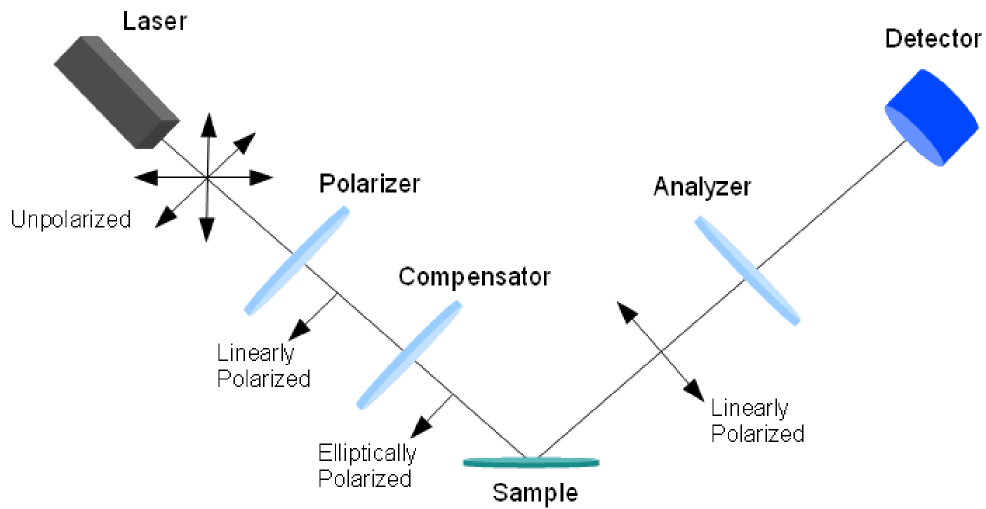

Figure 3.5: Typical setup for monochromatic ellipsometry.

Figure 3.5 illustrates a typical ellipsometry setup involving a source of collimated unpolarized light, a polarizer, an analyzer, a compensator and a photodetector. Light is initially emitted from a laser and is linearly polarized by the polarizer. The optional compensator changes the phase of the light causing elliptically polarized light to be incident on the sample. The reflected radiation passes through an optional second compensator and a polarizer. The second polarizer is called the analyzer. The basic ellipsometry setup shown in Figure 3.5 is used to measure ρ which is defined as

$$\rho = \frac{r_p}{r_s} = \tan(\Psi)e^{i\Delta} \quad (3.1)$$

where r_p and r_s are given by

$$r_p = \frac{n_1 cos\theta_0 - n_0 cos\theta_1}{n_1 cos\theta_0 + n_0 cos\theta_1} \quad (3.2)$$

$$r_s = \frac{n_0 cos\theta_0 - n_1 cos\theta_1}{n_0 cos\theta_0 + n_1 cos\theta_1} \quad (3.3)$$

Here θ_0 represents the angle of incidence, θ_1 is the angle of refraction, n_0 the RI of the incident or ambient medium and n_1 is the RI of the reflecting medium. Essentially, r_p is the ratio of the E-field amplitudes in the plane of incidence before and after reflection. r_s is a similar ratio, except using the E-field amplitude perpendicular to the plane of incidence. The measured values of Ψ and Δ cannot be converted directly into the optical constants of the sample, and a model analysis must be performed after the measurement [37].

The setup depicted in Figure 3.5 is for monochromatic ellipsometry. A broadband light source in combination with rotating elements can be used to obtain information over a wide spectral range. This method is called spectroscopic ellipsometry. For the purposes of this project, RI measurements in the telecommunications wavelength range were required, so spectroscopic infrared ellipsometry was used. In the past, this type of ellipsometry was conducted using a rotating component setup in combination with a grating spectrometer. This method is overly time consuming and unreasonable for real-time measurement. The use of a Fourier-Transform Spectrometer can resolve this issue. FTIR along with a rotating-analyzer ellipsometer can be combined to achieve infrared ellipsometry [38].

3.4 Transmission Electron Microscopy

The traditional light microscope has a limited resolution imposed by the wavelength of visible light. This limitation is one of the numerous reasons why the electron microscope is a more effective and powerful method for studying materials. The concept of the electron microscope was first proposed in 1932 by Knoll and Ruska, who successfully demonstrated that electron lenses could be used to produce electron images [39]. Only four years later, the first commercial transmission electron microscope (TEM) was realized by Metropolitan-Vickers. In the 1940s, commercial TEMs became widely available from various companies including Hitachi, JEOL, Philips and RCA [40].

Modern TEMs that are used today are capable of characterizing materials from the micrometer scale down to the subatomic scale.

Essentially, TEM involves a beam of high-energy electrons which is focused on a thin specimen using electro-magnetic lenses. The electron beam interacts with the specimen as it passes through. The transmitted electron beam contains information about the sample structure which is used to form an image. Figure 3.6 illustrates the two basic

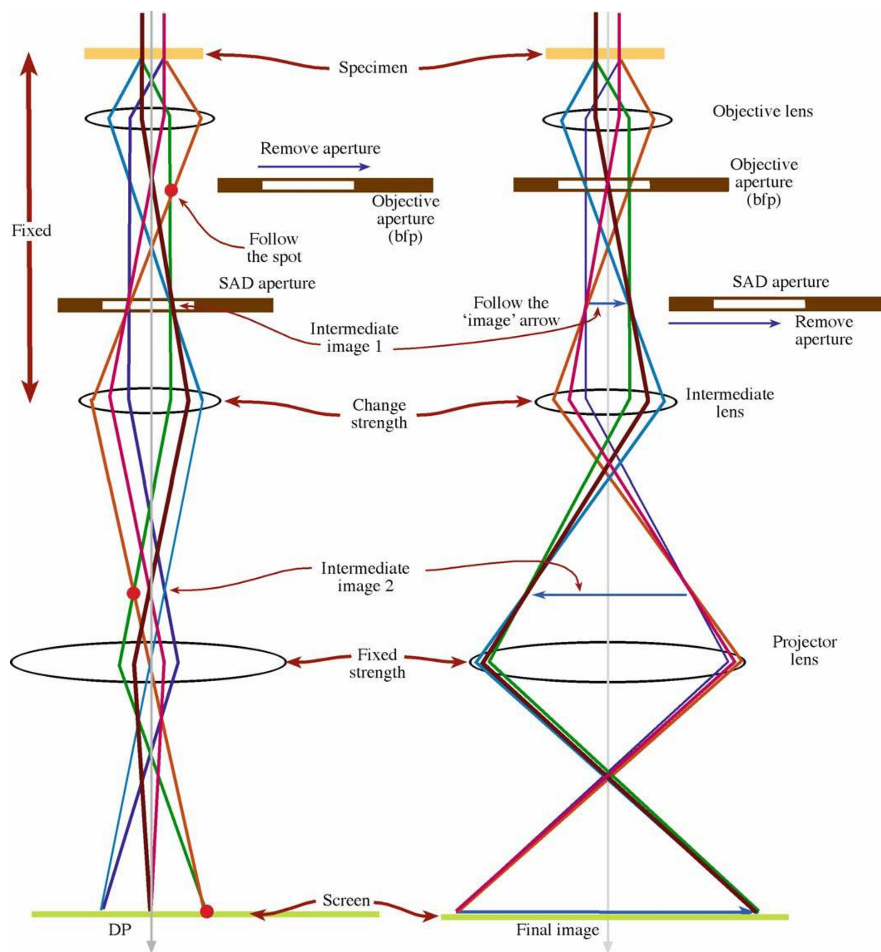

Figure 3.6: (Left) TEM schematic in diffraction mode. (Right) TEM schematic in imaging mode [40]

operations of the TEM imaging system, diffraction mode and imaging mode. Diffraction pattern analysis and other in-depth topics are not covered in this section as they are largely not applicable to this project. A detailed outline of TEM can be found in "*Transmission Electron Microscopy*" by Williams and Carter [40]. For the purposes of this project, TEM was used to obtain cross-sectional images of the resonant-cavity structures. Sample imaging was performed at the Canadian Centre for Electron Microscopy (CCEM) at McMaster University using the Philips CM12 Microscope, shown in Figure 3.7. The CM12 is a conventional analytic TEM operating at 120 kV.

Figure 3.7: Philips CM12 conventional analytic TEM operating at 120kV

Chapter 4

Modeling and Calibration Results

4.1 Resonant-Cavity Modeling

For the initial phase of this project, a computer model was developed in an effort to investigate the performance characteristics of resonant-cavity structures. The model was useful in determining how performance is influenced by minor variations of the physical parameters of the structures. The code for the model was written in Matlab using the transfer-matrix method outlined in Section 2.2.

Figure 4.1 depicts a multilayer thin-film structure consisting of alternating *a*-Si/SiO_2 layers. The thickness of each layer corresponds to one quarter of the optical path length at the primary wavelength (1550 nm), with the exception of the half-wave middle layer. The simulated reflectance spectrum of this structure is given in Figure 4.2. The result reveals a clear region of high reflectivity due to the periodic nature of the structure. The high index contrast of *a*-Si and SiO_2 enables near-unity reflectance in this region. As a result of the

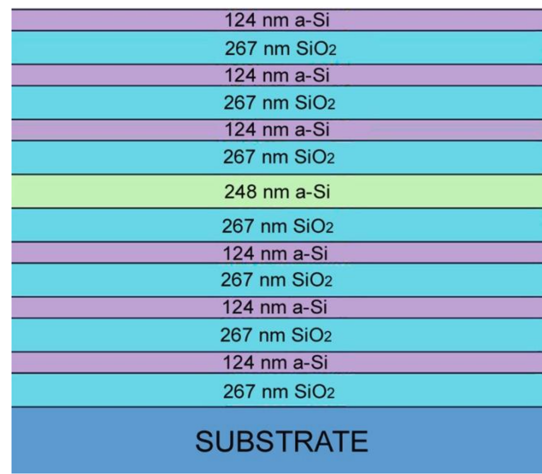

Figure 4.1: 14-layer resonant-cavity structure composed of alternating *a*-Si/SiO_2 layers.

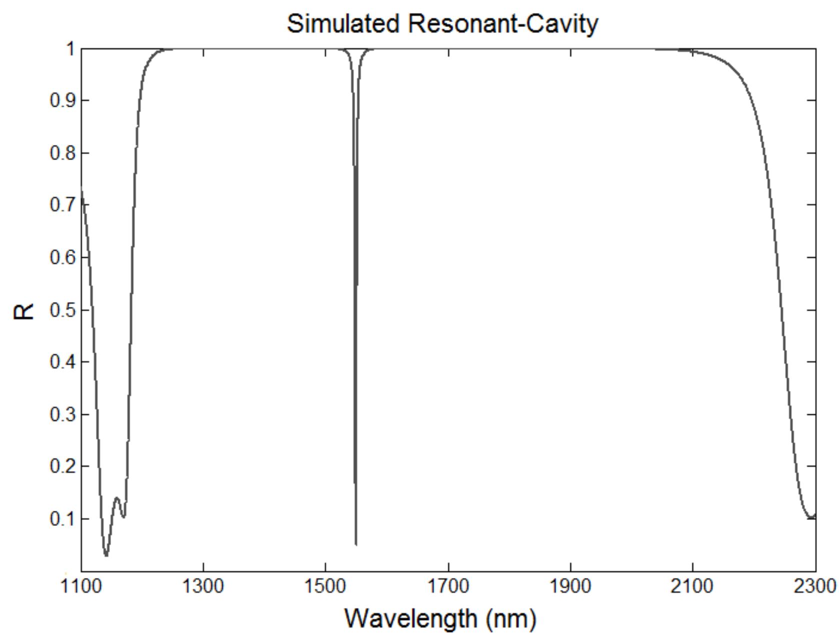

Figure 4.2: Simulated reflectivity spectrum for the structure depicted in Figure 4.1.

half-wave layer, a sharp dip in the reflectance or, in other words, a transmission peak, is present at the resonant wavelength of 1550 nm.

The reflectivity of the top and bottom mirrors can be controlled by altering the number of *a*-Si/SiO_2 periods. The addition of more periods results in a greater mirror reflectivity and an increase in overall quality of the structure. This is due to enhancement of the light field within the half-wave layer at the resonant wavelength. Given the high RI contrast, few periods are required to achieve high reflectivity within the resonance region. As demonstrated in Figure 4.2, a 14-layer structure will yield near-unity reflectivity over an 800 nm band. Such a design could therefore yield a highly efficient and wavelength-selective photodetector.

Figure 4.3 shows the effect of symmetrically decreasing the number of periods. If one period is subtracted from the top and bottom dielectric mirrors, near-unity reflectivity is maintained. However, the width of the transmission peak increases which would result in a less efficient detector. If only six layers are used, the reflectivity within the resonance region is significantly affected, and the transmission peak width is several times greater. The position of the transmission peak can be controlled by altering the thickness of the middle *a*-Si layer only. This effect is demonstrated in Figure 4.4 which depicts the simulated spectrum as the middle-layer thickness is varied from the ideal resonance thickness. It is evident that small changes in thickness yield a shift of the resonance wavelength without having a significant effect on the overall shape of the spectrum, even though the structure no longer has the ideal design for its specific resonant wavelength.

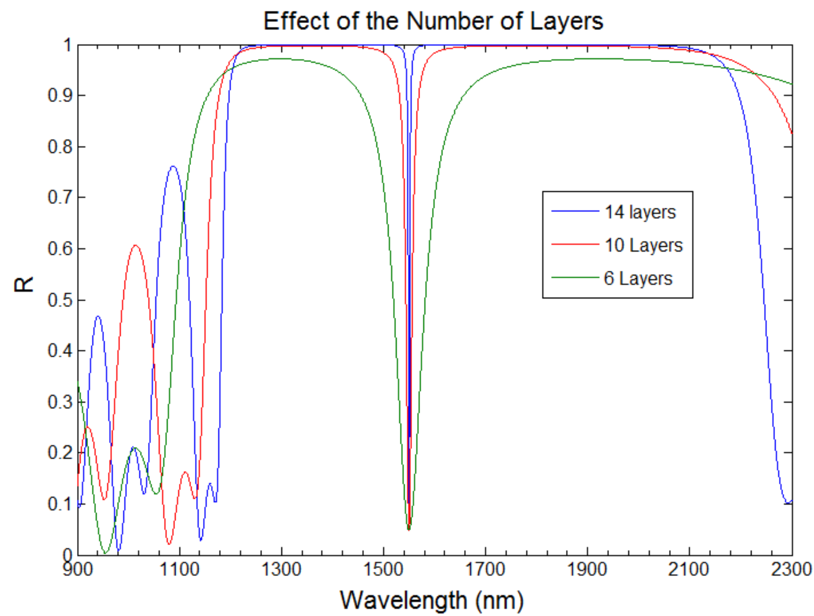

Figure 4.3: Comparison of simulated reflectivity spectra in relation to the number of layers.

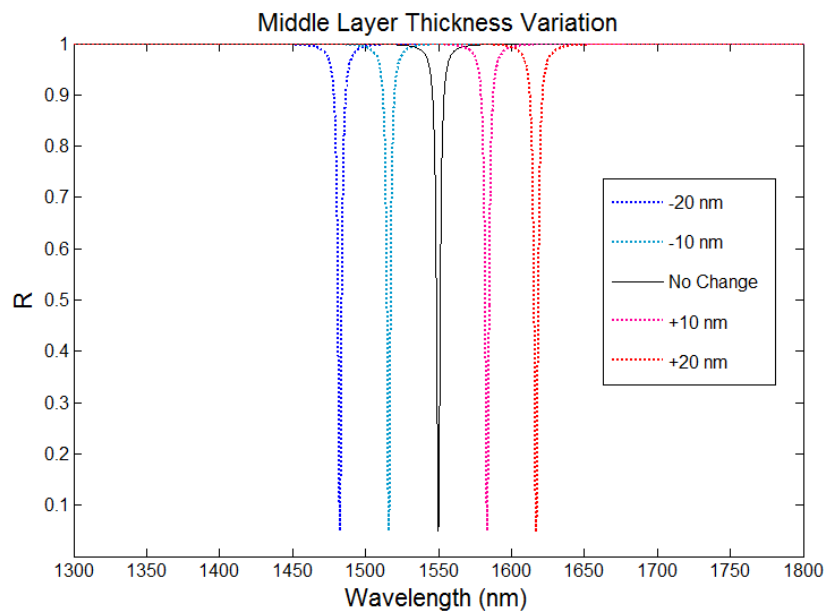

Figure 4.4: Simulated reflectivity spectra with varying thickness of the middle $_{a}$-Si layer.

If the middle-layer thickness is altered by a larger amount, the quality of the structure will be affected. This is demonstrated in Figure 4.5. Here, the thickness is increased by 40 nm intervals. After a total increase of 80 nm, the effect becomes apparent, as the transmission peak becomes wider. The detrimental effect is further magnified after a 120 nm increase.

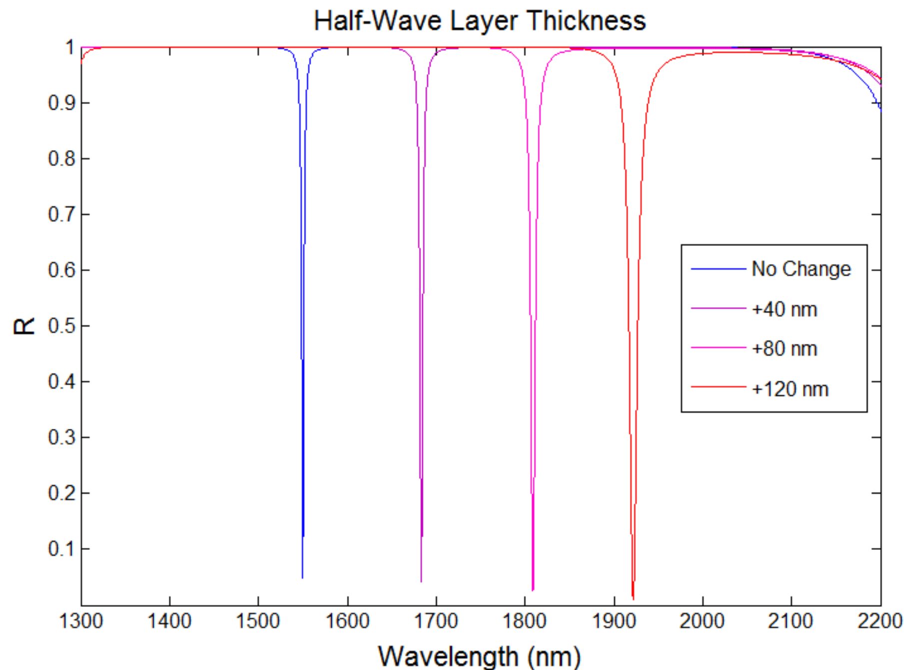

Figure 4.5: Simulated reflectivity spectra showing the detrimental effect of excess variation of the middle-layer thickness.

The simulated optical characteristics of these structures indicate that the level of efficiency enhancement can be increased by the addition of extra layers to the top and bottom mirrors. Figure 4.6 shows the simulated spectra for a random thickness variation of all layers between -10 nm and 10 nm. In this case the spectra may shift towards longer or shorter wavelengths depending on the overall structure thickness after the variation.

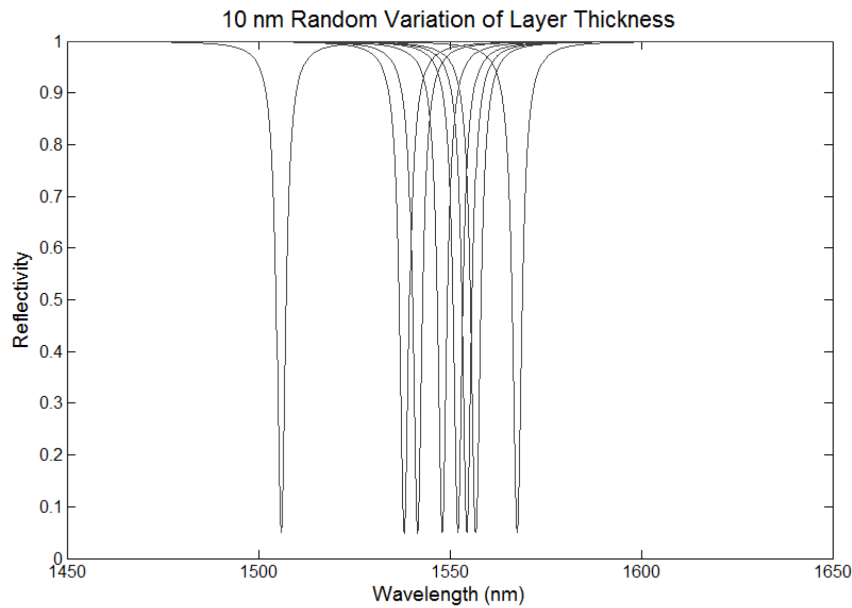

Figure 4.6: Simulated reflectivity spectra showing ±10 nm random variation of all layer thicknesses.

The extreme reflectance curve near 1500 nm corresponds to a structure wherein the average thickness variation was negative for both *a*-Si and SiO_2. A reflectance curve near 1600 nm will occur if the average thickness variation is positive.

4.2 Single-Layer Film Tests

A study of CVD-deposited *a*-Si and SiO_2 single-layer films was conducted as a preliminary step before the fabrication of the multilayer structures. The purpose of this step was to determine optimal deposition conditions and gain insight into how the materials will behave in a multilayer structure. Single-layer films of *a*-Si and SiO_2 were deposited on Si substrates at temperatures of 300°C, 500°C and 700°C. A portion of each

film was then annealed at 950°C for ten minutes to simulate the dopant activation which would be required to fabricate the eventual photodetector. The thickness and RI of the samples were measured using infrared ellipsometry.

For all *a*-Si films, the RI was found to be dependent on the deposition temperature, with an overall range of 2.6 - 3.3 at 1550 nm. The annealing step was found

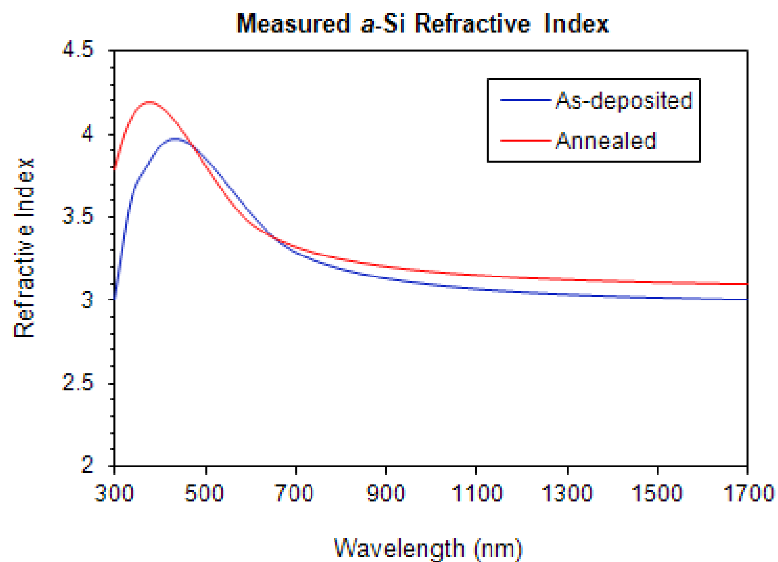

Figure 4.7: Measured RI for a single layer of *a*-Si deposited at 500ºC

to affect both the thickness and RI of all *a*-Si films, regardless of deposition temperature. An example of this effect is illustrated in Figure 4.7, which shows a clear refractive index change for the *a*-Si sample deposited at 500°C. The thickness of this film decreased by 12% after annealing.

The RI of SiO_2 films was also dependent on deposition temperature, with an overall range of 1.42 - 1.45 at 1550 nm. Again, the annealing step was found to alter the

thickness and RI of all SiO_2 films. Figure 4.8 shows a clear decrease in RI after annealing. The sample thickness decreased by 3% after annealing. Given the decrease in

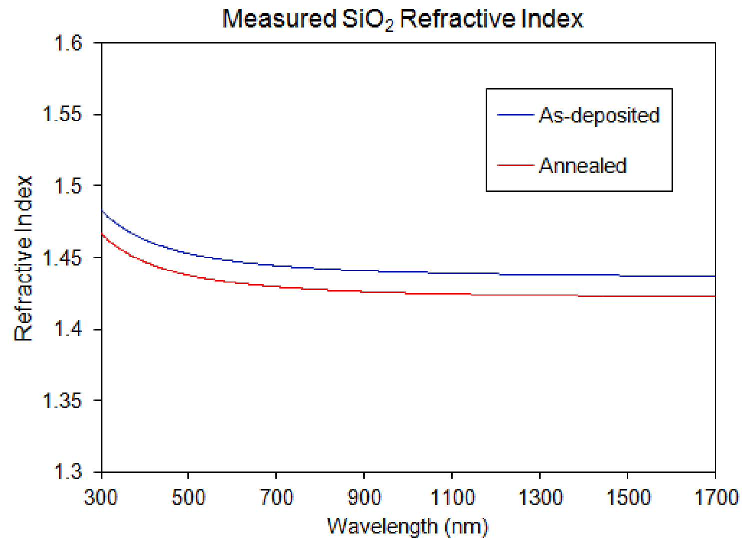

Figure 4.8: Measured RI for a single layer of SiO_2 deposited at 500ºC.

RI with annealing, additional tests must be conducted to determine how the density and other material properties are affected by annealing.

Overall, the annealing process had the least prominent effect on films deposited at 700°C. This was true for both *a*-Si and SiO_2 films. At this deposition temperature the RI for *a*-Si and SiO_2 was measured to be 3.13 and 1.45, respectively. These values were used as input in the computer model to simulate performance characteristics.

4.3 Discussion of Modeling and Calibration Results

The computer model was effective in demonstrating the optical characteristics of the resonant-cavity structure. According to the model, a 14-layer structure composed of

a-Si and SiO_2 will yield a sharp transmission peak at 1550 nm while maintaining near-unity reflectivity at other wavelengths within the range of 1200 nm - 2100 nm. Given these results, the resonant-cavity design described above could be utilized to fabricate a highly selective and efficient photodetector. The absorption region would have a thickness of only 248 nm, allowing the device to operate at higher speeds in comparison to conventional detectors which require thicker absorption regions to achieve good quantum efficiency. The modeling results also demonstrate the effect of using fewer *a*-Si/SiO_2 periods in the design. According to Figure 4.3, the removal of one period from the top and bottom mirrors will result in a wider transmission peak, while the reflectance elsewhere remains at near-unity. This design would still result in a high-efficiency detector, although the quality of the reflectance spectrum is inferior to the 14-layer design. If two periods are removed from each mirror, both the peak width and the high-reflectance region are negatively affected. For this reason, the project is focused on structures with either 10 or 14 layers.

The modeling results also provide insight into the impact of structural variations away from the ideal resonance design. An increase or decrease in the thickness of the middle layer causes the resonance peak to shift towards longer or shorter wavelengths, respectively. This effect becomes relevant in the fabrication phase where the exact layer thickness may depend on deposition conditions such as temperature and deposition time. The position of the resonance peak can therefore give insight into the nature and scale of any structural changes taking place during the deposition or during

post deposition processes such as annealing. Structural changes can be exploited as a mechanism to control the peak position. A small structural change could be intentionally employed in the design phase without necessarily redesigning the entire structure to be in accordance with the ideal resonance condition. According to Figure 4.5, the spectrum quality should be expected to decrease if the change in thickness is large enough.

The computer model of the resonant-cavity structure is able to accurately predict the reflectance spectra; however, it is essential to consider the existence of variations between the ideal model and physical structures. The refractive indices of both materials may not be uniform throughout the structure. The exact value may also differ slightly in comparison to the values chosen for the model. Inconsistencies may be present in the thicknesses of each layer, as well as the thickness along the length of a single layer.

Aside from the modeling results, the single layer test results were also valuable, primarily for the calibration of the multilayer structure depositions. Out of the three tested deposition temperatures, 700ºC yielded samples that were less affected by post-deposition annealing. This deposition temperature was therefore selected for all multilayer structures fabricated in this research. Although 700ºC is the optimal choice given the single-layer test results, the deposition rate is relatively slow at this temperature. Structures containing 14 layers require approximately 28 hours in the CVD chamber before completion.

Chapter 5

Device Analysis Results

5.1 Spectral Measurements Using FTIR

Figure 5.1 shows the design of the first fabricated structure. This 14-layer structure was deposited by ICP-CVD on a Si substrate at 700ºC. During the 28 hour deposition, the wafer was not removed from the vacuum chamber. The wafer was cleaved into two pieces, one of which was annealed in N_2 gas at 950ºC for 10 minutes.

Figure 5.1: 14-layer resonant-cavity structure deposited on a Si substrate at 700ºC

The reflectivity spectra for the as-deposited and annealed structures were measured at normal incidence and are plotted in Figure 5.2.

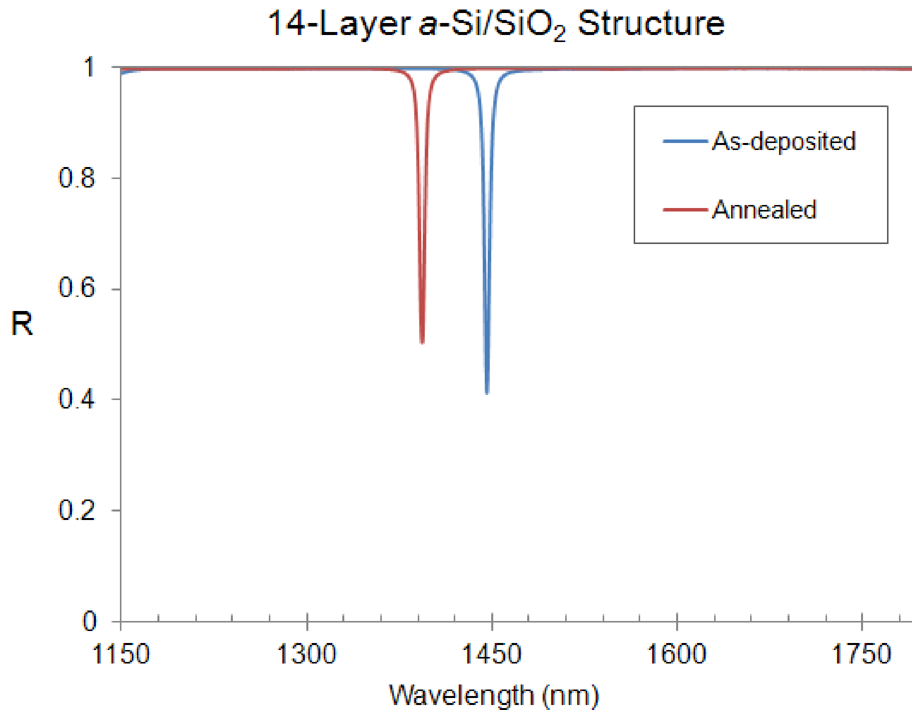

Figure 5.2: Measured reflectivity spectra for as-deposited and annealed samples of the resonant-cavity structure depicted in Figure 5.1.

The expected region of near-unity reflectivity is clearly present before and after annealing. For the as-deposited film, a sharp reflectivity minimum - or transmission peak - occurs at 1445 nm, with a FWHM of about 5 nm. At this wavelength, the film transmits 60% of the incident light. The transmission peak shifts to 1390 nm upon annealing. The transmittance is decreased by 10 percentage points for the annealed film. The optical characteristics of this film indicate the presence of a resonant cavity as intended.

However, the resonant wavelength is shorter than the design wavelength of 1550 nm. A similar 10-layer structure was fabricated using identical deposition conditions. The design for this structure is given in Figure 5.3. Once again, half of the deposited structure was annealed in N_2 at 950ºC for 10 minutes.

124 nm a-Si
267 nm SiO2
124 nm a-Si
267 nm SiO2
258 nm a-Si
267 nm SiO2
124 nm a-Si
267 nm SiO2
124 nm a-Si
267 nm SiO2
SUBSTRATE

Figure 5.3: 10-layer resonant-cavity structure deposited on a Si substrate at 700ºC

The reflectivity spectra for the as-deposited and annealed structures are plotted in Figure 5.4. In comparison to Figure 5.2, the transmission peaks have a larger width. This effect is a result of having two fewer periods and agrees with the results of the modeling section. For the as-deposited film, the transmission peak occurs at 1485 nm with a FWHM of about 16 nm. At this wavelength, the film transmits 75% of the incident light. The transmission peak shifts to 1450 nm upon annealing. The transmittance is decreased by 10 percentage points for the annealed film. These results indicate the presence of a resonant cavity; however the transmission peaks are again shifted to shorter wavelengths. For this

structure the transmission peaks are closer to the design wavelength of 1550 nm compared to the 14-layer structure.

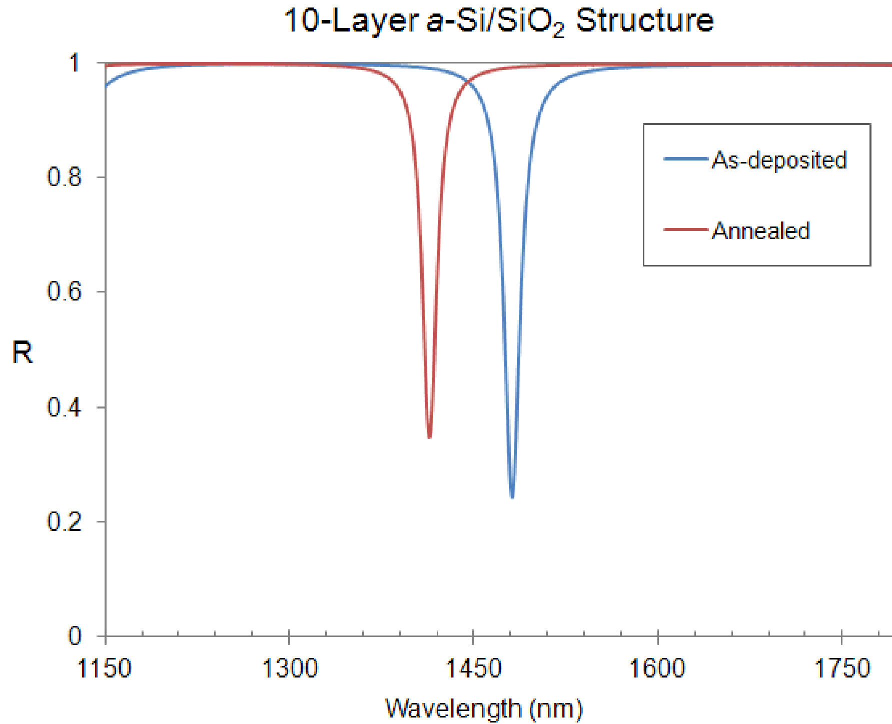

Figure 5.4: Measured reflectivity spectra for as-deposited and annealed samples of the resonant-cavity structure depicted in Figure 5.3.

.

5.2 TEM Imaging

The spectral plots presented in Figures 5.2 and 5.4 indicate that the transmission peaks of the resonant-cavity structures are initially shifted away from the design wavelength during the deposition and then shifted a second time by the annealing process.

In an effort to gain insight into the potential causes of the peak shifting, the structures were imaged using TEM.

A cross-sectional image of the 14-layer structure is presented in Figure 5.5. The image depicts a periodic structure with all 14 layers including the visibly wider half-wave layer. A section of the Si substrate is also visible at the bottom of the image. This image confirms that the structure was deposited correctly with no visible defects such as missing layers or large-scale deformation. The 10-layer structure was also deposited correctly with no visible defects present in the overall structure.

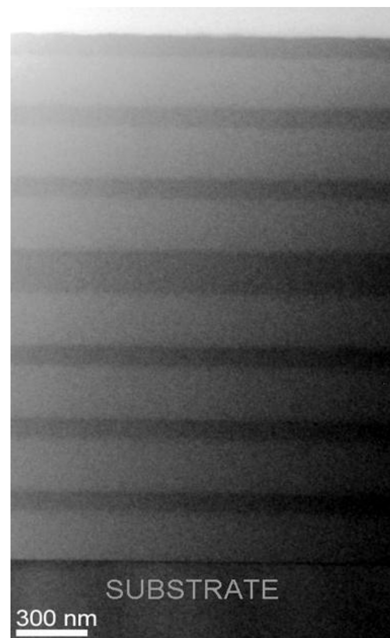

Figure 5.5: TEM image of the a 14-layer structure.

The magnification level was increased to study individual layers of *a*-Si and SiO_2. For the as-deposited structures the layer thicknesses of both materials were less than the designed thickness. For the annealed structures, all layers were found to be thinner in comparison to the as-deposited structures. As a quantitative example, the middle *a*-Si layer lost 12% thickness during the deposition due to the long duration and high temperature. An additional 2% was lost during the anneal. The effect was significantly less prominent for SiO_2 layers.

Figure 5.6 depicts a magnified section of the 10-layer structure. The image reveals some roughness along the layer interfaces. The roughness was not impacted by the annealing process. A further magnified image of the layer interface is presented in Figure 5.7.

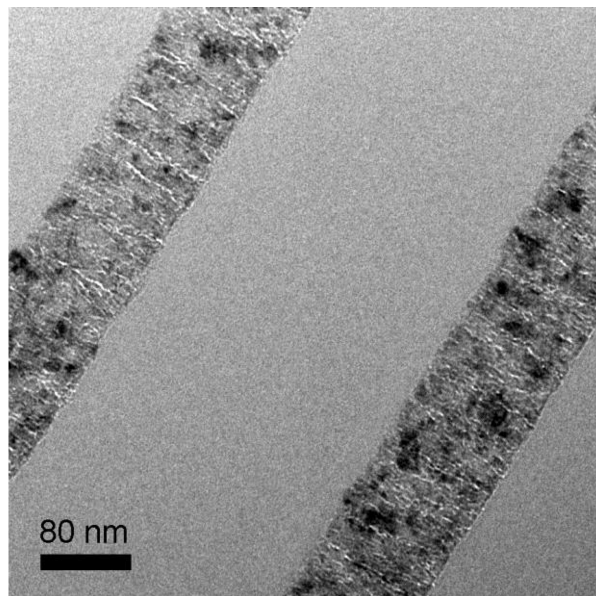

Figure 5.6: TEM image showing a three-layer section of the resonant cavity structure. The darker layers are *a*-Si.

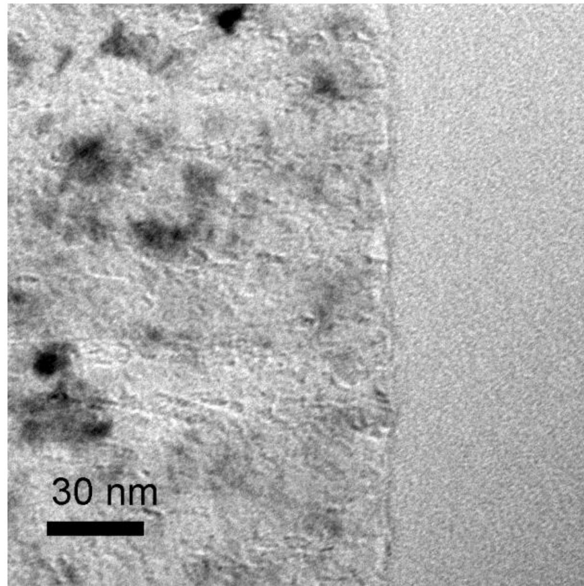

Figure 5.7: TEM image of the *a*-Si/SiO_2 layer interface.

5.3 Thickness Compensation

The results presented in Section 5.2 indicate a significant reduction in the thickness of the individual layers of the resonant-cavity structures compared to the design values both in the as-deposited and annealed state. To counteract these changes, a compensation technique was tested whereby one or more layers were deposited with added thickness to compensate for losses during the deposition and annealing processes. The required thickness to be added to each layer was estimated using the results from the TEM analysis in combination with the computer model. As a first attempt, a 14-layer structure was deposited wherein the thickness of every layer was increased. This method

yielded a structure with a transmission peak at a wavelength more than 200 nm longer than the design wavelength. By altering all layers including the middle *a*-Si layer, both the peak position and the overall spectrum are shifted. Due to the shift, it is difficult to maintain control over the resonance position using this method. A second approach is to compensate using the middle layer only. Although this approach requires a more significant thickness change, it also enables a higher level of control. Using this approach, a resonant-cavity structure with a resonance peak at the desired wavelength was successfully fabricated. The reflectance spectrum for this structure is given in Figure 5.8. With a transmission

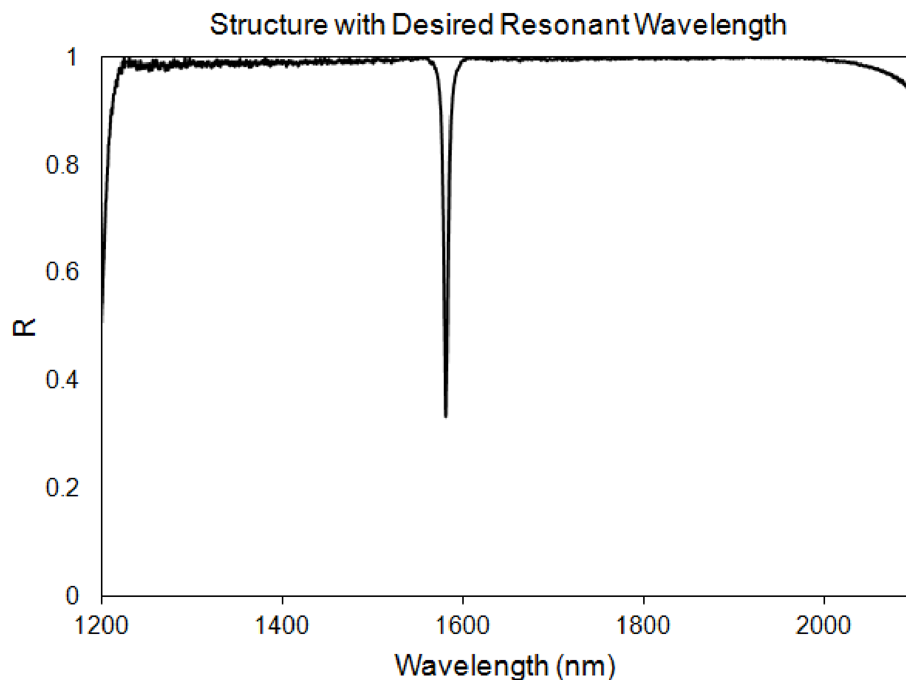

Figure 5.8: Measured reflectivity spectrum for the thickness-compensated structure.

peak at 1585 nm, this structure is a good candidate for a photodetector operating in the telecommunication wavelength range, given that the peak will shift to a value near 1550 nm during the dopant activation process.

5.4 Discussion of Structure Analysis Results

The FTIR analysis of the resonant cavity structures was effective in revealing the reflective properties over a wide wavelength range. The initial 14-layer structure yielded promising results which demonstrate the capacity for potential enhancement of a photodetector. As predicted by the model, the reflectance was 100% within the band surrounding the resonance peak. The detector would therefore be unresponsive within this band. The presence of a sharp resonance peak indicates enhancement of the light field within the half-wave *a*-Si layer due to multiple passes of light in this region. The same result was found for the 10-layer structure, which also exhibited near-unity reflectance along with a sharp resonance peak. Both structures transmitted greater than 50% of light at the respective resonant wavelengths. This property is likely dependent on several factors including the smoothness of the layer interfaces and the presence of inter-layer diffusion, both of which affect the overall quality of the structure. It is probable that the high temperature and long duration of the deposition have a deteriorating effect on the overall quality of the structure. The effect is less prominent for the 10-layer structure, likely because the deposition time is shorter. The annealing process furthers this effect,

which is evident in the reflectivity spectra of both structures. After annealing, both structures see a 10 percentage point decrease in transmission at resonance while the peak width remains constant.

The resonance peaks for all deposited structures were shifted towards shorter wavelengths than intended in the design. It can be concluded that part of the shifting occurs during the deposition, while the annealing process is the cause of the remainder of the shift. The single-layer test results outlined in section 4.2 show that annealing at 950°C for 10 minutes does have a minor effect on the thickness and RI of both materials. This result explains the peak shifting during annealing. Although the temperature of the deposition is lower than the annealing temperature, the deposition process likely has a similar effect on the materials given its long duration. The TEM images confirm that the individual layers are, in fact, thinner than intended both after the deposition and the annealing processes. The magnified images of the individual layers also reveal minor variations in the uniformity of the layer interfaces. Some non-uniformity is also visible within the *a*-Si layers. These non-uniformities affect the amount of light transmitted at resonance. Further tests are needed to determine the magnitude of the effect.

Chapter 6

Temperature Sensing Applications

6.1 Background

Fiber optic sensors have become widely applied in place of traditional electrical sensors, which are highly susceptible to harsh environments [41]. If a fiber optic system is used, the opto-electronic interface of the sensor can be separated from the potentially hostile measurement environment. Therefore, sensors can be fabricated that are immune to electromagnetic interference and can be employed in the presence of flammable gases. Self-heating errors in RF fields can be eliminated by using dielectric materials only. A common type of temperature sensor is based on the Fabry-Perot interferometer. For this sensor, the interferometer is typically a thin platelet of material linked to the end of an optical fiber. The RI of the interferometer material must be temperature dependent so that the interference characteristics and overall spectrum vary with temperature. The Fabry-Perot sensor can provide a compact and rugged method of wavelength encoded temperature measurement. Temperature sensing by means of a Fabry-Perot etalon was first demonstrated by Christiensen in 1974 [42]. In that study, multilayer dielectric

mirrors were deposited on both surfaces of a 3.3 mm thick slab of glass. A temperature of range of 150 K was achieved.

A simple Si-based Fabry-Perot sensor can be fabricated using a single slice of single-crystalline Si which is electrostatically bonded between two thicker pieces of Pyrex glass. Such a design is commercially available from Photonetics [43]. For this temperature sensor, the glass-encased silicon etalon is directly bonded to a glass capillary containing an optical fiber. The output spectrum is split into separate components above and below the resonant wavelength. Temperature determination is based on the ratio of the intensities of the separate components. Other approaches to fiber based temperature sensing can be found in references [44-48].

The cost-efficiency of Si-based Fabry-Perot detectors can be improved by depositing the material directly on the end face of an optical fiber. This method has previously been demonstrated by Schultheis *et al*. who initially deposited an *a*-Si layer on the tip of a fiber [49]. The *a*-Si layer was then crystallized using an argon-ion laser. A single layer of Si_3N_4, followed by a layer of aluminum, were then deposited to form the secondary mirror, with the primary mirror being the fiber/silicon interface. Komatsu *et al*. demonstrated a band pass filter deposited on an optical fiber end face. For the presented system, a measurement accuracy of ±0.5ºC was achieved [50].

The resonant-cavity structures fabricated for this study are composed of materials with RIs that are sensitive to temperature. For these structures, a small RI variation will alter the optical path length within each layer which affects the overall interference of

light as it propagates within the structure. If the change is sufficiently small, the transmission peak will continue to exist with only its position altered. Although the multi-layer films in this project were deposited on a Si substrate, the same structures could be deposited on the end face of an optical fiber. This approach would require a recalibration of the deposition for room temperature given that the ICP-CVD is not capable of accurately heating an optical fiber to a consistent temperature of 700°C throughout the deposition process.

6.2 Sensitivity Tests

The computer model used to determine the optical properties of the resonant-cavity structures was modified to include temperature sensitive indices. Figure 6.1 shows the simulated results of a 14-layer structure as the temperature is increased by intervals of 15°C. As the temperature increases, the transmission peak is shifted towards longer wavelengths. The overall shape of the peak is unaffected within this temperature range.

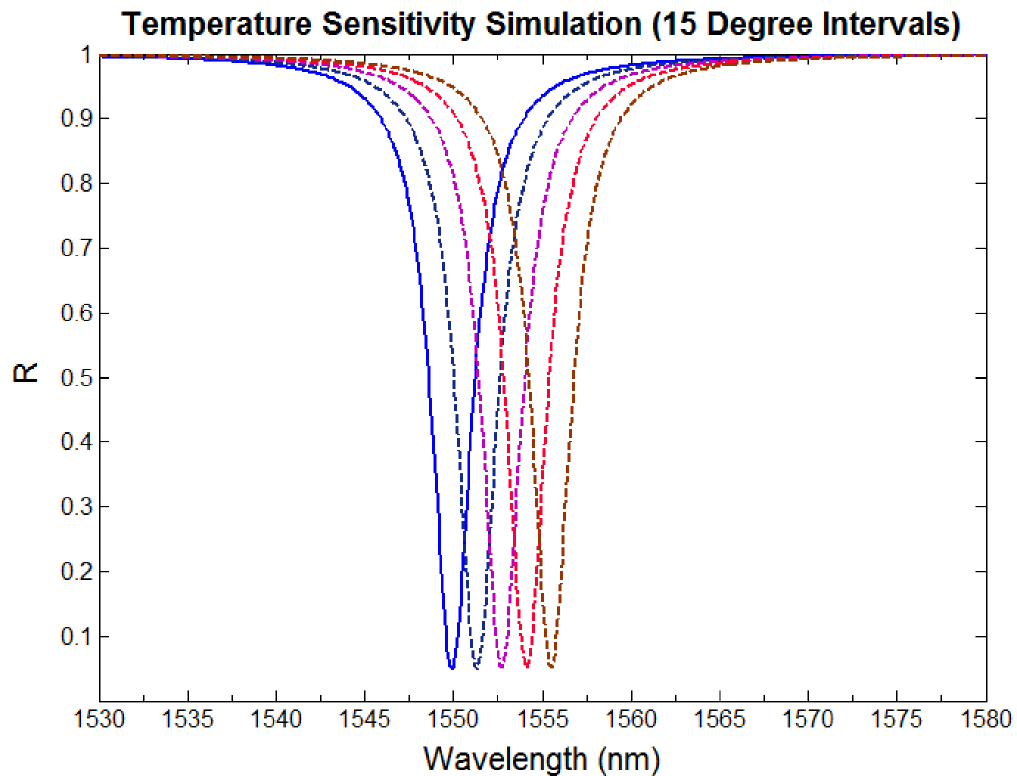

Figure 6.1: Simulated temperature sensitivity of the resonant-cavity structure using 15 degree intervals.

Temperature sensitivity of the resonant-cavity structures was tested using an apparatus depicted in Figure 6.2. The infrared light source is a tunable laser with a scanning range from 1525 nm to 1550 nm at a resolution of 0.1 nm. An optical fiber directs the output beam to the sample which rests horizontally on a hot plate. Light that is reflected back from the sample is directed in to the power monitor. Scanning and data collection are computer controlled using LabVIEW software.

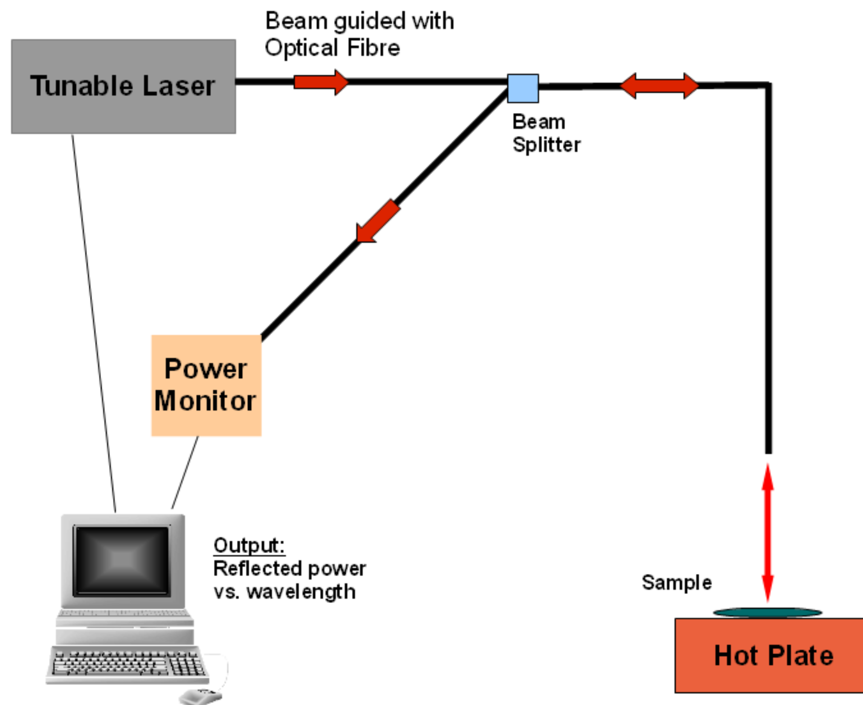

Figure 6.2: Tunable laser setup used for temperature sensitivity testing.

Figure 6.3 shows the measured spectrum of a 14-layer structure as the sample temperature was increased in 15°C intervals. At each temperature level, the sample temperature was allowed to stabilize before measurement. The structure exhibits a clear sensitivity to temperature, indicating minor changes in the resonance conditions. Within this temperature range, the peak was shifted an average of 0.5 nm towards longer wavelengths for each 15 degree temperature interval. The position of the transmission peak at room temperature was not found to be permanently altered by the heating process. More tests are required to determine the maximum temperature at which the device can maintain its original spectrum without it being permanently altered.

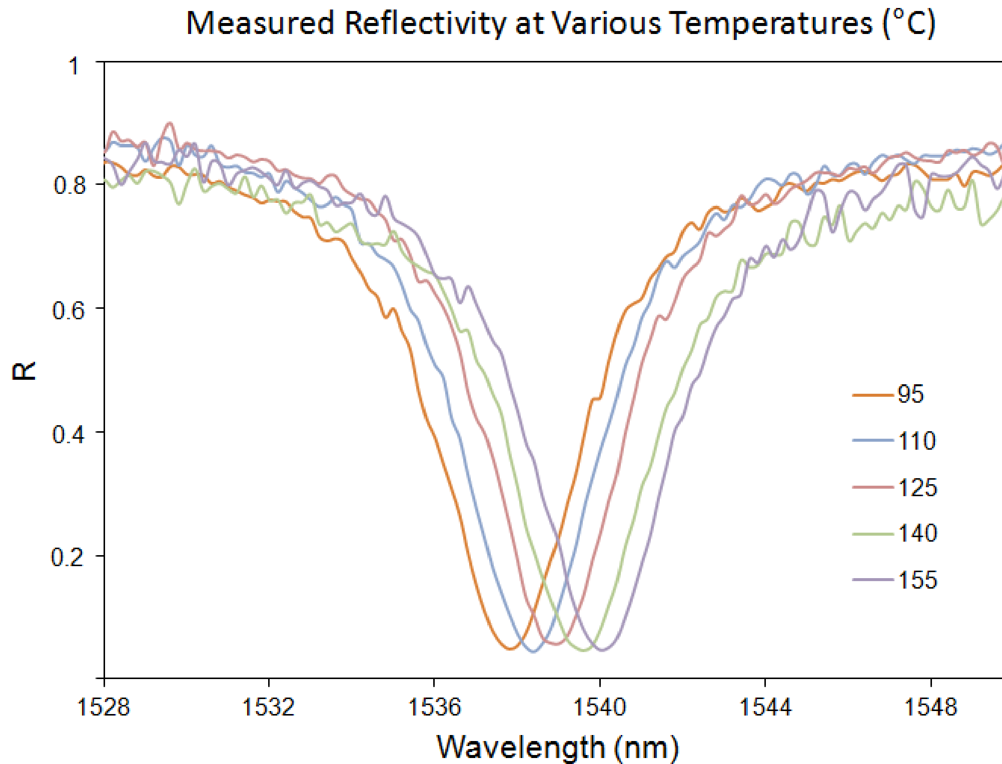

Figure 6.3: Measured reflectivity spectra of the resonant-cavity structure with increasing temperature.

6.3 Discussion of Temperature Sensitivity Results

The temperature sensitivity tests indicate that the specific type of resonant-cavity structures fabricated in this research may be of interest for sensing applications. According to the model, the reflective and transmissive properties of such structures are altered as the temperature is varied, due to changes in the refractive indices of the materials. Temperature changes are therefore translated to changes in the exact position

of the resonance. This effect was verified experimentally as depicted in Figure 6.3. For both modeling and experimental results, the resonance peak shifted towards longer wavelengths by consistent intervals without any significant alteration of the general shape of the reflectivity spectrum. This property would allow for simple and reliable wavelength-encoded temperature measurement. It should be noted that the magnitude of the change in peak position was less pronounced for the experimental case in comparison to the model. This inconsistency is likely related to the thermo-optic coefficients of the materials which were not measured experimentally and were assumed to be in exact agreement with book values for Si and SiO_2. The thermo-optic coefficients may have been altered during the deposition due to the high temperature and long duration in the CVD chamber. This dependence is likely related to the hydrogen content in the deposited films, which may impact the thermo-optic coefficients.

It should be noted that the measurement environment surrounding the sample was not isolated from the temperature of the laboratory. Therefore, a temperature gradient likely will have been present between the surface of the sample and the back side of the wafer in contact with the hot plate. The temperature of the sample was also assumed to be equal to the hot plate temperature. As an improvement, a more effective heating system could be employed to directly monitor and control the sample temperature. The alignment of the beam with the sample surface is another potential source of error. The beam was assumed to be normally incident on the sample, given that the reflected light was required to return directly to the optical fiber from which it was delivered. A proper alignment

system could be employed to ensure normal incidence and eliminate any peak shifting related to oblique angles.

Aside from temperature sensing, the structures may also have applications for tunable optical filters. Tunable components such as optical filters and other wavelength managed devices are in increasing demand for WDM networking. Examples of research activities in this area since 2000 can be found in [51-57].

Chapter 7

Conclusion and Future Work

This project provided some of the essential groundwork for further development of the RCE infrared photodetector. The optical characteristics of the resonant-cavity structures were initially investigated in the modeling phase. The simulations confirm that by careful selection of the layer thicknesses, a resonant-cavity structure composed of *a*-Si and SiO_2 can be designed to yield a sharp transmission peak at precisely 1550 nm, while maintaining near-unity reflectivity at other wavelength within the range of 1200 nm to 2100 nm. The impact of structural variations was also investigated using the developed model. Results reveal that minor changes in layer thicknesses cause a shift in the resonance wavelength. At 1550 nm, a 10 nm change in the middle layer thickness will result in a 30 nm shift of the resonance wavelength. The width of the resonance peak was determined to be dependent on the number of layers on the top and bottom mirrors. According to the model, a 10-layer structure is sufficient to achieve near-unity reflectivity in the resonance region of the spectrum. However, more periods could be implemented to decrease the peak width and thereby enhance the quantum efficiency of the detector. In the calibration phase, a study of single layer *a*-Si and SiO_2 films revealed that a

deposition temperature of 700°C produces samples that are less affected by post-deposition annealing in comparison to lower deposition temperatures. However, these samples are not immune to minor changes in thickness and RI caused by annealing.

The CVD-deposited multilayer structures exhibit the capacity for enhancement of a photodetector, primarily in the realm of efficiency, speed and wavelength selectivity. For all deposited structures, near-unity reflectance was achieved within the resonance band surrounding the transmission peak. In each case, a sharp resonance peak was observed, indicating enhancement of the light field within the half-wave *a*-Si layer. The percentage of light transmitted at resonance was greater than 50% for both 10-layer and 14-layer structures. This value is largely a function of the overall quality of the structure. It is probable that the conditions of the deposition and annealing processes affect the structure quality.

The FTIR analysis in combination with TEM imaging revealed that the individual layers are less thick than intended, which explains the shifting of the resonance peak towards shorter wavelengths. The design was then altered to include 30 nm of extra thickness for the half-wave layer. Using this compensation technique, a structure was fabricated with the desired resonance wavelength. Although this final structure has a resonance peak at 1585 nm, the dopant activation process will shift the peak closer to the intended operating wavelength of 1550 nm. Therefore, this research phase was successful in providing an appropriate CVD "recipe" which can be re-used to fabricate identical

structures for further research towards the RCE photodetector operating at the telecommunications wavelength of 1550 nm.

The multilayer-structure design was also investigated for potential temperature sensing applications. The initial sensitivity tests results indicate that this type of structure could be of interest for sensing applications. The temperature-dependent RI of *a*-Si and SiO_2 cause the interference conditions to be altered as the temperature is varied, resulting in a tunable resonant wavelength. This effect was verified by computer simulation and experimentation, although the magnitude of the effect was less prominent for the experimental case. The resonance peak was shifted towards longer wavelengths by consistent intervals without any significant change to the general shape of the spectrum. This property would allow for reliable wavelength encoded temperature measurement.

The next phase of the photodetector development process involves using ion implantation to dope the resonant-cavity structure with Boron and Phosphorus. An appropriate dopant activation temperature should be determined by testing the carrier concentration levels of doped samples that have been annealed at a range of temperatures between 700°C and 1000°C. The model should also be modified to include absorption in the half-wave layer, which can be achieved by integrating the imaginary part of the RI in the transfer-matrix calculations. The model will help determine the appropriate number of layers to be used on the top and bottom mirrors to optimize absorption. At maximum absorption, the lifetime corresponding to the absorption in the half-wave layer is matched to the total time during which light exists within the structure. If the number of periods on

the top mirror are too few, the time corresponding to the coupling in of light is less than that of absorption; the absorption at resonance is less than 100% and the remaining light is coupled back out of the cavity before being absorbed (i.e. reflected). If the number of periods is too large, the absorption lifetime is less than the time of the coupling process. This means that not all of the light is coupled in, resulting in a broadening of the absorption band and a decrease in the peak absorption level.

Figure 7.1 depicts the structure after upper-layer etching and before ion implantation. To allow for maximum collection, the electrode must penetrate into the absorbing region. An effective method to accomplish this is through interdigitated n+ and p+ doped regions. These regions are shown in Figure 7.2 with the upper layers removed for clarity.

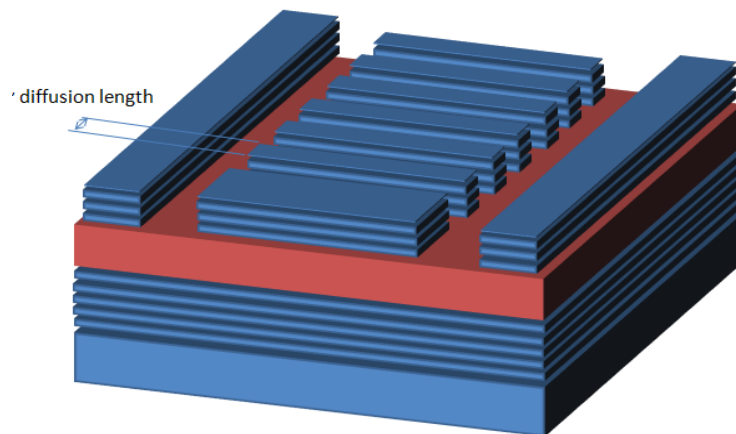

Figure 7.1: Resonant-cavity structure after upper-layer etching.

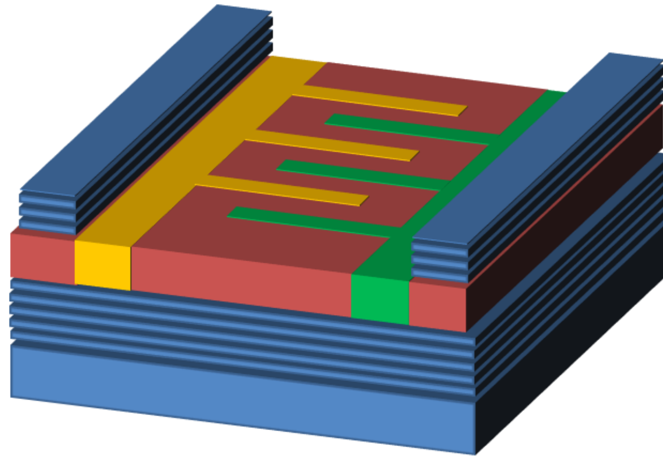

Figure 7.2: Resonant-cavity structure with upper layers removed for clarity, revealing interdigitated doped regions.

This design allows for an arbitrarily large area to be nearly completely depleted, so that all generated carriers may be extracted efficiently. The doped regions do not have a dielectric stack above them, so light will not tend to be confined in these regions.

The temperature sensitivity tests conducted for this research would ideally be refined to further investigate the possible temperature sensing applications. Sources of error originating from the experimental setup and procedure should be reduced to improve the accuracy of the results. Additional tests should be conducted to further evaluate the sensing capability of the resonant-cavity structures. The range of sensitivity is a property of interest which should be determined. Also of interest is the maximum temperature that the structure can withstand without undergoing any permanent structural changes or spectral alterations. It was evident from the deposition that lengthy exposure at 700°C will have a permanent impact on the spectrum. It can therefore be concluded that

the threshold temperature for these structures is below 700°C. Another key sensing characteristic that should be determined in future testing is the minimum temperature change that can be accurately detected by the structure.

As previously discussed, fiber optic sensors are highly advantageous in comparison to traditional electric sensors. The resonant cavity structure should therefore be implemented in conjunction with an optical fiber which would serve to transmit the signal from the potentially harsh sensing environment to the optoelectronic interface. This arrangement could be achieved by depositing the multilayer film structure directly on the optical fiber end face. By this method, the fabrication is primarily confined to one stage with no requirement for bonding after the deposition. Such a deposition is possible using the ICP-CVD system, however, the heating system which maintains the wafer temperature is not equipped to accurately heat an optical fiber. For the purposes of future research, the deposition must be recalibrated for room temperature.

References

[1] C. Li, Q. Yang, H. Ou, and Q. Wang, "Fabrication of Silicon-on-Reflector for Si-Based Resonant-Cavity-Enhanced Photodetectors," *IEEE Electron. Compon. Technol. Conf.*, pp. 1486-1488, 2000.

[2] M. Gokkavas et al., "High-speed high-efficiency large-area resonant cavity enhanced p-i-n photodiodes for multimode fiber communications," *IEEE Photonics Technol. Lett.*, vol. 13, no. 12, pp. 1349-1351, 2001.

[3] A. Ramam, G.K. Chowdhury, and S. J. Chua, "An approach to the design of highly selective resonant-cavity-enhanced photodetectors," *Appl. Phys. Lett.*, vol. 86, no. 17, 2005.

[4] B.M. Onat et al., "100-GHz resonant cavity enhanced Schottky photodiodes," *IEEE Photon. Technol. Lett.*, vol. 10, no. 5, pp. 707-709, 1998.

[5] N. E. J. Hunt, E. F. Schubert, and G. J. Zydzik, "Resonant-cavity p-i-n photodetector utilizing an electron-beam evaporated Si/SiO2 microcavity," *Appl. Phys. Lett.*, vol. 63, no. 3, pp. 391-393, 1993.

[6] O.I. Dosunmu, D.D. Cannon, M.K. Emsley, L.C. Kimerling, and M.S. Unlu, "High-speed resonant cavity enhanced Ge photodetectors on reflecting Si substrates for 1550-nm operation," *IEEE Photon. Technol. Lett.*, vol. 17, no. 1, pp. 175-177, 2005.

[7] K. Kishino et al., "Resonant cavity-enhanced (RCE) photodetectors," *IEEE J. Quantum Electron.*, vol. 27, no. 8, pp. 2025-2034, 1991.

[8] M.S. Unlu, M.K. Emsley, O.I. Dosunmu, P. Muller, and Y. Leblebici, "High-speed Si resonant cavity enhanced photodetectors and arrays," *ournal of Vacuum Science and Technology A: Vacuum, Surfaces and Films*, vol. 22, no. 3, pp. 781-787, 2004.

[9] M.S. Unlu and S. Strite, "Resonant cavity enhanced photonic devices," *J. Appl. Phys.*, vol. 78, no. 2, pp. 607-639, 1995.

[10] M.S. Unlu, "Resonant-cavity-enhanced devices improve efficiency," *Optoelectronics World Magazine*, vol. 34, no. 3, pp. 15-20, 1998.

[11] J.J. Goedbloed and J. Joosten, "Responsivity of avalanche photodiodes in the presence of multiple reflections," *Electron. Lett.*, vol. 12, no. 14, pp. 363-364, 1976.

[12] E. Ozbay et al., "High-speed >90% quantum-efficiency p–i–n photodiodes with a resonance wavelength adjustable in the 795–835 nm range," *Appl. Phys. Lett.*, vol. 74, no. 8, pp. 1072-1075, 1999.

[13] N. Biyikli et al., "45-GHz Bandwidth-Efficiency Eesonant-Cavity-Enhanced ITO-Schottky Photodiodes," *IEEE Photon. Technol. Lett.*, vol. 13, no. 7, pp. 705-707, 2001.

[14] T. Knodl et al., "RCE photodetectors based on VCSEL structures," *IEEE Photon. Tech. Lett.*, vol. 11, no. 10, pp. 1289-1291, 1998.

[15] Y.M. El-Batawy and M.J. Deen, "“Resonant Cavity Enhanced Photodetectors (RCE-PDs): structure, material, analysis and optimization," in *Proc. SPIE Quantum Sensing: Evolution and Revolution From Past to Future*, 2003, pp. 363-378.

[16] M.S. Unlu, G. Ulu, and M. Gokkavas, "Resonant Cavity Enhanced Photodetectors," in *Photodetectors and Fiber Optics*, H. S. Nalwa, Ed. N: Academic Press, 2001, ch. 2, pp. 97-201.

[17] C. Lenox et al., "Resonant Cavity InGaAs-InAlAs Avalanche Photodiodes with Gain-Bandwidth Product of 290 GHz," *Photon. Technol. Lett.*, vol. 11, no. 9, pp. 1162-1164, 1999.

[18] J. Kovac et al., "InAlGaAs-InGaAs-InP RCE pin photodiode 1300 nm wavelength region," in *Eigth International Conference on Indium Phosphide and Related Materials*, Schwabisch-Gmund, 1996, pp. 219-222.

[19] M.S. Unlu, K. Kishino, H.J. Liaw, and H. Morkoc, "A theoretical study of resonant cavity-enhanced photodectectors with Ge and Si active regions," *J. Appl. Phys.*, vol. 71, no. 8, pp. 4049-4058, 1992.

[20] S.S. Murtaza, H. Nie, J.C. Campbell, J.C. Bean, and L.J. Peticolas, "Short-wavelength, high-speed, Si-based resonant-cavity photodetector," *IEEE Photon. Tech. Lett.*, vol. 8, no. 7, pp. 927-929, 1996.

[21] Y. Shi, J.H. Zhao, J. Sarathy, G.H. Olsen, and H. Lee, "Resonant cavity enhanced heterojunction phototransistors based on GaInAsSb-AlGaAsSb grown by molecular beam epitaxy," *IEEE Photon. Technol. Lett.*, vol. 10, no. 2, pp. 258-260, 1998.

[22] A. Chin and T. Y Chang, "Enhancement of quantum efficiency in thin photodiodes through absorptive resonance," *J. Lightwave Technol.*, vol. 9, no. 3, pp. 321-328, 1991.

[23] R. Kuchibhotla et al., "Low-voltage high-gain resonant-cavity avalanche photodiode," *IEEE Photon. Technol. Lett.*, vol. 3, no. 4, pp. 354-356, 1991.

[24] J. Bowers and C., Jr. Burrus, "Ultrawide-band long-wavelength p-i-n photodetectors," *J. Lightwave Technol.*, vol. 5, no. 10, pp. 1339-1350, 1987.

[25] Z.-M. Li et al., "Analysis of a resonant-cavity enhanced GaAs/AlGaAs MSM photodetector," *IEEE Photon. Technol. Lett.*, vol. 4, no. 5, pp. 473-476, 1992.

[26] W. Qiming, L. Cheng, C. Buwen, and Y. Qinqing, "Si-based resonant-cavity-enhanced photodetector," in *Proceedings of SPIE*, vol. 4225, 2000, pp. 107-111.

[27] M. K. Emsley and M. S. Unlu, "Epitaxy-Ready Reflecting Substrates for Resonant-Cavity-Enhanced Silicon Photodetectors," in *Proc. IEEE Lasers and Electro-Optics Society*, vol. 2, 2000, pp. 432–433.

[28] M. S. Unlu et al., "Application of optical resonance to biological sensing and imaging II: resonant cavity biosensors," in *Biophotonics: Biological and Medical Physics, Biomedical Engineering*, L. Pavesi and P.M. Fauchet, Eds.: Springer, 2008.

[29] F.L. Pedrotti and L.S. Pedrotti, *Introduction to Optics*, 2nd ed. New Jersey: Prentice Hall, 1993.

[30] H.O. Pierson, *Handbook of chemical vapor deposition*. Park Ridge (NJ), 1992.

[31] J. Hopwood, "Review of inductively coupled plasmas for plasma processing," *Plasma Sources Sci. Technol.*, vol. 1, no. 2, p. 109, 1992.

[32] D. L. Flamm, "Processes depending on plasma discharges sustained in a helical resonator," 5,304,282, Apr. 19, 1994.

[33] H. Zhang, "Study of the optimal deposition conditions for an inductively coupled plasma chemical vapour deposition (ICP-CVD) system," McMaster University, 2005.

[34] A. Rothen, "The Ellipsometer, an Apparatus to Measure Thicknesses of Thin Surface Films," *Rev. Sci. Instrum.*, vol. 16, no. 2, pp. 26-30, 1945.

[35] P. Drude, *The Theory of Optics*. New York: Drover, 1959.

[36] D. Gonçalves and E.A. Irene, "Fundamentals and Applications of Spectroscopic Ellipsometry," *Quím. Nova*, vol. 25, no. 5, 2002.

[37] J. H. W. G. den Boer, "Spectroscopic Infrared Ellipsometry: Components, Calibration and Application," *Eindhoven University of Technology*, 1995.

[38] M. Schubert, *Infrared ellipsometry on semiconductor layer structures: phonons, plasmons, and polaritons*. Berlin Heidelberg: Springer-Verlag, 2004.

[39] M Knoll and E Ruska, "Das Elektronenmikroskop (Electron Microscope)," *Z. Phys.*, vol. 78, pp. 318-339, 1932.

[40] D.B. Williams and C.B. Carter, *Transmission Electron Microscopy: A Textbook for Materials Science*. New York: Springer, 1996.

[41] T.G. Giallorenzi et al., "Optical Fiber Sensor Technology," *Microwave Theory and Techniques*, vol. 30, no. 4, pp. 472-511, 1982.

[42] D.A. Christensen, "Temperature Measurement Using Optical Etalons," in *Annual Meeting of the Optical Society of America*, Houston, 1974.

[43] J.C. Hartl, E.W. Saaski, and G.L. Mitchell, "Fiber optic temperature sensor using spectral modulation," in *Proc. SPIE 838*, San Diego, 1987, pp. 257-262.

[44] D. Hohlfeld and H. Zappe, "An all-dielectric tunable optical filter based on the thermo-optic effect," *J.Opt. A: Pure Appl. Opt.*, vol. 6, pp. 504-511, 2004.

[45] C. A. Musca et al., "Monolithic Integration of an Infrared Photon Detector With a MEMS-Based Tunable Filter," *IEEE Electron Device Lett.* , vol. 26, no. 12, pp. 888-890, 2005.

[46] D. Hohlfeld and H. Zappe, "Thermal and Optical Characterization of Silicon-Based Tunable Optical Thin-Film Filters," *IEEE J. Microelectromech. Syst.*, vol. 16, no. 3, pp. 500-510, 2007.

[47] W. Zhang, J.F. Tao, W.M. Zhu, H. Cai, and A. Q. Liu, "Tunable Optical Filter by Thermal Effect Based on MEMS Technology," *Adv. Mater. Res.*, vol. 74, pp. 315-318, 2009.

[48] P. Xu, F. Pang, N. Chen, Z. Chen, and T. Wang, "Fabry-Perot temperature sensor for quasi-distributed measurement utilizing OTDR," in *Optical Fiber Sensors Conference*, Chengdu, 2008, pp. 1-4.

[49] L. Schultheis, H. Amstutz, and M. Kaufmann, "Fiber-Optic Temperature Sensing With Ultrathin Silicon Etalons," *Opt. Lett.*, vol. 13, p. 782, 1988.

[50] Y.Komatsu, K. Inoue, M. Nakano, and S. Onoda, "Optical fiber temperature sensor using a thin film band pass filter and dual wavelength push-pull reflectometry," in *Proc. SPIE*, vol. 7004, 2008.

[51] L. Domash, E. Ma, N. Nemchuk, A. Payne, and M. Wu, "Tunable thin film filters," in *Proc. of OFC*, vol. 2, 2003, pp. 522-524.

[52] R. Parmentier et al., "Towards tunable optical filters," in *Proc. Optical Interference Coatings*, Banff, 2001.

[53] L. Domash, M. Wu, N. Nemchuk, and E. Ma, "Tunable and Switchable Multiple-Cavity Thin Film Filters," *J. Lightwave Technol.*, vol. 22, no. 1, p. 126, 2004.

[54] L. Domash, E. Ma, N. Nemchuk, A. Payne, and M. Wu, "Tunable thin films based on thermo-optic semiconductor films," in *Proc. SPIE*, vol. 4833, 2002.

[55] R. Parmentier and M. Lequime, "Substrate-strain-induced tunability of dense wavelength-division multiplexing thin-film filters," *Opt. Lett.*, vol. 28, pp. 728-730, 2003.

[56] J. Floriot, F. Lemarchand, and M. Lequime, "Tunable double-cavity solid-spaced bandpass filter," *Opt. Expres*, vol. 12, pp. 6289-6298, 2004.

[57] M.K. Emsley, O.I. Dosunmu, and M.S. Unlu, "High-speed resonant-cavity-enhanced silicon photodetectors on reflecting silicon-on-insulator substrates," *IEEE Photon. Technol. Lett.*, vol. 14, no. 4, pp. 519-521, 2002.